

Validation of the FE and RB Implementation of the DwarfElephant-Package on the Basis of Diffusion Controlled Temperature and Pressure Benchmarks

Bachelor-Thesis

Deadline: 30.09.2018

**Computational Geoscience and Reservoir Engineering
(CGRE)**

Name: Tobias Ganther
Student ID: 354742
Bachelor Program: Applied Geoscience
First Examiner: Prof. Florian Wellmann, Ph.D
Second Examiner: Dr. Simon Virgo
Supervisor: Denise Degen, M.Sc.

Contents

List of Figures	II
List of Tables	III
1 Introduction	1
2 Theory	2
2.1 Fourier's Law	2
2.1.1 Governing Equation / PDE	2
2.1.2 Thermal Conductivity	3
2.1.3 Thermal Conductivities of Different Rock Types	4
2.2 Darcy's Law	4
2.2.1 Governing Equation / PDE	4
2.2.2 Hydraulic Conductivity and Permeability	5
2.2.3 Assumptions for Darcy's Law	6
2.3 Theis Solution	8
2.3.1 Governing Equations	8
2.3.2 Assumptions	9
2.4 Finite Element Method	9
2.4.1 Processing	10
2.5 Reduced Basis Method	11
3 Model	12
4 Methodology	13
4.1 Fourier	13
4.2 Darcy	16
4.3 Theis Solution	18
5 Results	18
5.1 Fourier	18
5.2 Darcy	27
5.3 Theis Solution	35
6 Discussion	37
7 Conclusion	40
8 Outlook	40
9 References	42
A Additional Contents	45
A.1 Theis W(u) Table	45
A.2 Homogeneous steady state Plots	46
A.3 Python Code for Theis Solution	50

List of Figures

1	Heat Transfer through a Slab (Turcotte, 2014)	3
2	Different Types of Material in the Earth and associated Mechanisms of Heat Transport (Clauser, 2011)	3
3	Histograms of thermal Conductivity for (a) sedimentary, (b) volcanic, (c) plutonic, and (d) metamorphic Rocks (Clauser, 2009) .	5
4	Upper (a) and Lower (b) borderline Situation for Darcy's Law (Hermance, 1999)	7
5	Different Types of Elements (habituatingfea.blogspot.com)	10
6	Mesh which represents a Mug (MOOSE.org)	11
7	Sketch of the applied Model for both geologic Formations	12
8	Fourier Plot of the FE and RB Node Values plotted against the Depth (seperated)	20
9	Fourier Plot of the FE and RB Node Values plotted against the Depth (combined)	21
10	Difference Plot shown from the side with the highest positive Temperature Difference between FE and RB	22
11	Difference Plot shown from the side with the highest negative Temperature Difference between FE and RB (displayed by 180 Degree compared to Fig.10)	22
12	Steady State Fourier Difference Plot, upper Regions of the Surfaces sliced down	23
13	Slice normal to the x-axis on the steady Fourier Simulation	24
14	Slice normal to the y-axis on the steady Fourier Simulation	24
15	Slice normal to the z-axis on the steady Fourier Simulation	25
16	Transient Fourier Temperature Plot ($dt = 0.2$), Temperature in [-] .	26
17	Transient Fourier Temperature Plot ($dt = 1.6$), Temperature in [-] .	26
18	Plot of the transient FE Temperature simulation, first and last timestep are shown	27
19	Darcy Plot of the FE and RB Node Values plotted against the Depth (seperated)	28
20	Darcy Plot of the FE and RB Node Values plotted against the Depth (summarised)	29
21	Darcy steady state Pressure Difference Plot shown from the left Side in Front	30
22	Darcy steady state Pressure Difference Plot shown from the right Side in Front	30
23	Steady State Darcy Difference Plot, upper Regions of the Surfaces sliced down, left side in Front	31
24	Slice normal to the x-axis on the steady Darcy Simulation	32
25	Slice normal to the y-axis on the steady Darcy Simulation	32
26	Slice normal to the z-axis on the steady Darcy Simulation	33
27	Transient Darcy Pressure Plot ($dt = 0.01$), Pressure in [-]	34
28	Transient Darcy Pressure Plot ($dt = 0.1$), Pressure in [-]	34
29	Plot of the transient FE Darcy Simulation, first and last Timestep are shown	35
30	Drawdown Curves for a predefined Aquifer mady by the Python Script	36

31	Plot of a Drawdown Curve calculated by Python and manually calculated Solutions	38
32	Steady State Fourier Difference Plot for the homogeneous Simulation	46
33	Slice normal to the x-axis on the homogeneous steady Fourier Simulation	46
34	Slice normal to the y-axis on the homogeneous steady Fourier Simulation	47
35	Slice normal to the z-axis on the homogeneous steady Fourier Simulation	47
36	Steady State Darcy Difference Plot for the homogeneous Simulation	48
37	Slice normal to the x-axis on the homogeneous steady Darcy Simulation	48
38	Slice normal to the y-axis on the homogeneous steady Darcy Simulation	49
39	Slice normal to the z-axis on the homogeneous steady Darcy Simulation	49

List of Tables

1	Typical Values for the Natural Permeabilities of Geologic Materials (Turcotte, 2014)	6
2	Values of the Analytical homogeneous Fourier steady State Solution	19
3	Values of the Analytical 3 layer Fourier steady State Solution	19
4	Values of the Analytical steady state homogeneous Darcy Solution	27
5	Values of the Analytical steady state 3 layer Darcy Solution	27
6	Predefined Aquifer Parameters used for the Validation of the Theis Solution	36
7	W(u) Values calculated by the Python Script vs. W(u Values from Literature) for certain u Values	36
8	Manually calculated Radial Distances and the respective Drawdowns	37
9	W(u) Values for different u Values (Rüde, 2015)	45

1 Introduction

Computer simulations are used to imitate real-world processes or systems in order to study dynamic behaviors in an environment that may be difficult to implement in real life. [1].

They are used in many branches of science and engineering, e.g. for weather modelling [2], economy [3], medicine [4] and even for military purposes [5].

Computational modelling and simulation have been identified as key factors for success both in research and product development. But the integration of software tools and management of digital models and computational data are still limiting factors in the wide application of such computational methods. There is a clear trend of research in the area of data, simulation and knowledge management and there is still plenty of requirement for further research [6].

In earth science computer simulations are getting more relevant as well e.g. for petroleum and geothermal reservoir engineering. The use of simulations is so extensive that simulations can be seen as a standard procedure nowadays [7][8].

The simulators enable a prediction of reservoir performance, although this task becomes immensely difficult when dealing with complex reservoirs that can arise from variation in formation and fluid properties. The complexity of the reservoirs has always been handled with increasingly advanced approaches [7].

New advances are adopted quickly and have also found application in related areas such as nuclear waste storage, environmental remediation and studies of the vadose zone [8].

There is a lot of commercial software for many branches of geoscience from companies (such as Schlumberger Software) as well as multiple freewares mostly for research purposes such as the MOOSE framework. MOOSE stands for “Multiphysics Object-Oriented Simulation Environment”. It was primarily developed by Idaho National Laboratory. It provides a high-level interface to some of the most sophisticated nonlinear solver technology on the plane [9]. The simulations performed for this thesis were made in MOOSE as well.

Doctoral candidate Denise Degen M.Sc. developed a package for the MOOSE framework. Its purpose is the solution of any kind of physics that is elliptic or parabolic and can be described as a partial differential equation (PDE). The main use of the package however is to provide a userfriendly acces to the Reduced Basis Method (RB) in MOOSE which originally uses the Finite Element Method (FEM / FE). The package is called "DwarfElephant".

Goal of the RB implementation of the package is to drastically decrease the computing time of computationally intensive simulations with a minimal loss of quality compared to the FEM.

The motivation of the thesis is the validation of the FE and RB implementation of the DwarfElephant-Package on the basis of diffusion-controlled temperature and pressure benchmarks. Therefore, multiple simulations are performed for different geologic cases using both FE and RB. The pressure and temperature distribution based on Darcy's and Fourier's Law are being simulated. The results of the FE and RB simulations are plotted against each other using Python and Paraview plots. Furthermore, the analytical solutions of the simulations are calculated as well. Using these plots potential errors in the simulation itself should be identified. But most importantly, the differences between the FE and RB results are inspected for the validation. The error between FE

and RB must not exceed a certain range of tolerance in order to provide decent results for RB. If the error range is not exceeded, the validation will be positive and the DwarfElephant-Package can be used to perform its purpose. After the validation, the Theis well function as a additional potential application and its implementation into DwarfElephant is discussed.

In Chapter 2 the necessary theoretical basics of the physical processes as well as FE and RB are the central topic. In Chapter 3 the used models and their production are explained. Chapter 4 describes the necessary pre- and postprocessing steps for the simulations followed by the results in Chapter 5. These results will be discussed in Chapter 6 and in Chapter 7 a final conclusion of the validation process is made. The last chapter is an outlook for further possible steps for the DwarfElephant-Package, especially the implementaion of the Theis Solution.

2 Theory

The following section offers a basic overview about the governing equations necessary to understand the work and the results of the thesis which are being discussed in the following chapters.

2.1 Fourier's Law

2.1.1 Governing Equation / PDE

The law of heat conduction, also known as Fourier's law, describes the conductive heat transport. It states that the heat flow, also known as the heat flux, is directly proportional to the negative temperature gradient [10].

$$q = -k\nabla T. \quad (1)$$

$$\begin{aligned} q &= \text{heat flux } [Wm^{-2}] \\ k &= \text{thermal conductivity } [Wm^{-1}K^{-1}] \\ T &= \text{temperature } [K] \end{aligned}$$

However, temperature measurements are mostly performed along vertical profiles in boreholes. Therefore only the vertical component of the temperature gradient is generally known [11]. In this case the equation can also be described for one dimension, where y is the vertical axis.

$$q = -k \frac{dT}{dy}. \quad (2)$$

In this example from Fig.1,(where l is the length of the slab) it can be written as:

$$q = \frac{k\Delta T}{l}. \quad (3)$$

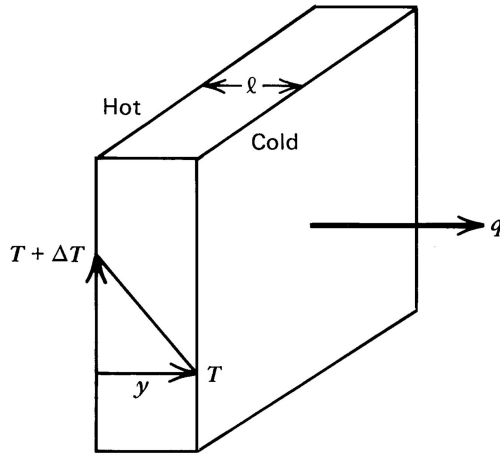


Figure 1: Heat Transfer through a Slab (Turcotte, 2014)

2.1.2 Thermal Conductivity

The coefficient k (also referred as λ) is the coefficient of thermal conductivity [10]. The thermal conductivity can be separated in two major parts. One of them is the scattering of quantized lattice vibrations, the phonons and the second part is the diffusive radiation of photons. These two processes are described by phonon thermal conductivity λ_p and radiative thermal conductivity, λ_r . The sum of them is termed as effective thermal conductivity, λ_{eff} [12]. In Figure 2 these mechanisms of heat transport get associated with materials which can be found in the earth.

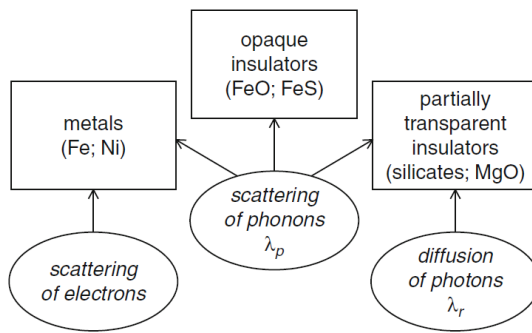


Figure 2: Different Types of Material in the Earth and associated Mechanisms of Heat Transport (Clauser, 2011)

The thermal conductivity can be measured directly on rock samples. There are numerous transient and steady state techniques for measuring thermal con-

ductivity [11].

If there are no rock samples, indirect measurements can be used as well. It is possible to make an estimation from the mineralogical composition and saturating fluids in the underground. It is also possible to use other physical properties such as porosity or bulk density [10].

2.1.3 Thermal Conductivities of Different Rock Types

There are plenty of thermal conductivity data available classified according to rock name and origin. Due to the heterogenous properties of rocks such as porosity, saturation, or mineral composition, there is a huge variability of thermal conductivity even within the same rock types [11]. This is the reason why the rock type is a very poor descriptor for physical properties. This limits the usefulness of collected data to regional levels, where certain measured rock samples were collected.

The thermal conductivity of minerals and rocks varies with the temperature and pressure. It also varies with the rocks porosity and the type of saturating fluid [13]. Depending on the basic rock types the variation of certain physical properties affects the thermal conductivity in a different scale. Figure 3 illustrates these differences in histograms for different rock types. The thermal conductivity of sedimentary rocks is mainly controlled by porosity and the sediment type. For volcanic rocks, porosity is the most influencing factor for the thermal conductivity. Plutonic and metamorphic rocks are generally much less porous. Here, the controlling factor is the dominant mineral phase. For plutonic rocks, the feldspar content determines the thermal conductivity. Rocks with a high feldspar content show a lower mean conductivity compared to rocks with low feldspar content. In spite of these differences, the means and medians for both distributions are nearly identical. For metamorphic rocks, the quartz content controls the thermal conductivity [12].

The heat conduction is the dominant transport process in the earth's crust when fluids flows are absent. For most crustal and mantle rocks, heat radiation becomes significant only at temperatures above 1200°C. In rocks with a higher proportion of glass, especially volcanic rocks or obsidian, heat radiation can already become significant at temperatures above 300°C [13].

2.2 Darcy's Law

2.2.1 Governing Equation / PDE

Darcy's law is an equation that describes the flow of a fluid through a porous medium. The flow through a porous medium is linearly proportional to the applied pressure gradient and inversely proportional to the viscosity of the fluid. It is an empirical relationship credited to Henry Darcy, who carried out experiments on the flow of water through vertical homogeneous sand filters in 1856 [10]. Darcy's Law has also been derived from the Navier–Stokes equations using homogenization [14].

$$u = -\frac{k}{\mu} \frac{dp}{dx}. \quad (4)$$

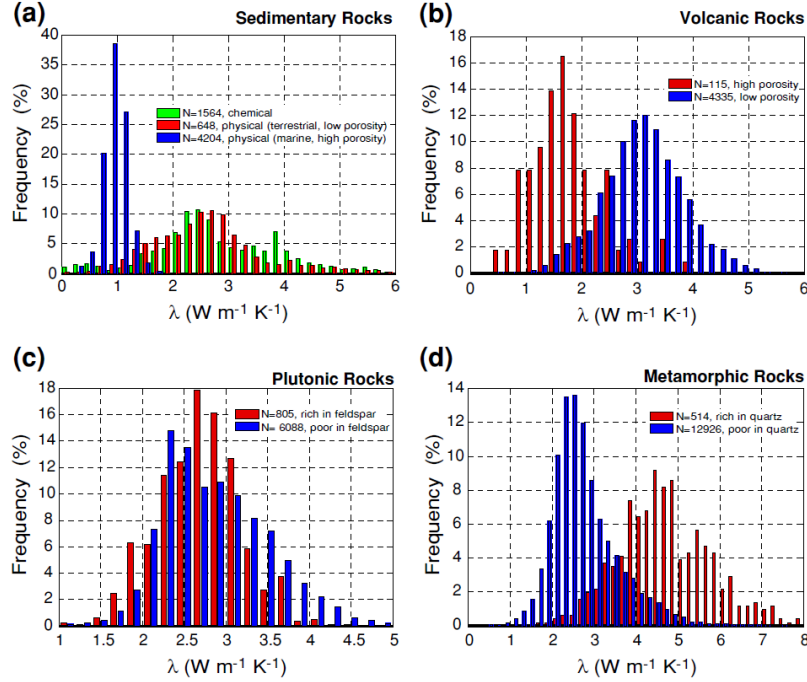


Figure 3: Histograms of thermal Conductivity for (a) sedimentary, (b) volcanic, (c) plutonic, and (d) metamorphic Rocks (Clauser, 2009)

$u = \text{flow rate per unit area } [\text{ms}^{-1}]$

$k = \text{hydraulic permeability } [\text{m}^2]$

$\mu = \text{dynamic viscosity of the fluid } [\text{m}^2 \text{s}^{-1}]$

$p = \text{pressure } [\text{pa}]$

Darcy's law can also be written in terms of the hydraulic head H:

$$u = -\frac{k\rho g}{\mu} \frac{dH}{dx}. \quad (5)$$

$g = \text{gravitation constant } [\text{ms}^{-2}]$

$\rho = \text{fluid density } [\text{kgm}^{-3}]$

$H = \text{hydraulic head } [\text{m}]$

2.2.2 Hydraulic Conductivity and Permeability

The permeability describes the ease with which a fluid can flow through a porous media. The higher the k – value the higher the permeability. Sediments with a high grain size are very permeable (also referred as pervious) while unfractured,

homogeneous rocks or clays are almost impermeable (impervious) as can be seen in Table 1 [10].

Table 1: Typical Values for the Natural Permeabilities of Geologic Materials (Turcotte, 2014)

Permeability K [m^2]	Classification	Material
10^{-7}		
10^{-8}		Gravel
10^{-9}	Pervious	
10^{-10}		
10^{-11}		Sand
10^{-12}		
10^{-13}	Semipervious	
10^{-14}		Sandstone
10^{-15}		
10^{-16}		Limestone
10^{-17}		
10^{-18}	Impervious	
10^{-19}		
10^{-20}		Granite

K is also known as hydraulic conductivity. It stands in a direct correlation to the hydraulic permeability [10].

$$K = \frac{k\rho g}{\mu}. \quad (6)$$

The hydraulic conductivity can be measured through various ways. One method is the measurement in the field with pump tests. It is also possible to measure the hydraulic conductivity through laboratory tests with permeameters [15]. Another way is the use of grain size curves using the correlation between grain size and hydraulic conductivity [16].

2.2.3 Assumptions for Darcy's Law

Darcy's law is only valid under certain conditions. First, the scale of porosity must be small compared to the other characteristic dimensions of the aquifer like the thickness. Another crucial factor is the necessity of a laminar flow in the medium [10]. The characteristics of the flow are measured by the Reynolds Number [15].

$$Re = \frac{Ud\rho}{\mu}. \quad (7)$$

Re = Reynolds number [-]

ρ = fluid density [kgm^{-3}]

U = filtration rate [ms^{-1}]

d = effective grain diameter [mm]

μ = dynamic viscosity of the fluid [m^2s^{-1}]

For the effective grain diameter the d_{10} is commonly used. It is measured by grading curves.[15]. The filtration rate does not represent the real flow velocity in the aquifer. The mean effective flow velocity (also described as velocity through the pores) is used to describe the real velocity in the aquifer. For its calculation the filtration rate and the effective porosity are needed. The normal flow velocity gets calculated by the following equation [17]:

$$v_n = \frac{v_f}{n_e}. \quad (8)$$

v_n = normal flow velocity [$m s^{-1}$]

v_f = filtration rate [$m s^{-1}$]

n_e = effective porosity [-]

A laminar flow is given for Reynolds Numbers under 10 for porous media (for channels a laminar flow is still given for numbers up to 2000). For numbers over 10, the flow becomes increasingly turbulent (flows over the Reynolds Number of 100 are exclusively turbulent). A higher filtration velocity increases the Reynolds Number. High hydraulic gradients can cause such an increase due to a higher amount of potential energy at the same distance compared to smaller gradients resulting in a higher filtration velocity. For low hydraulic gradients, especially in low permeable clay, Darcy is not valid as well. The 'resistance' of the low permeable rocks prevents a flow from happening for lower gradients. A fluid flow occurs after reaching the threshold pressure.

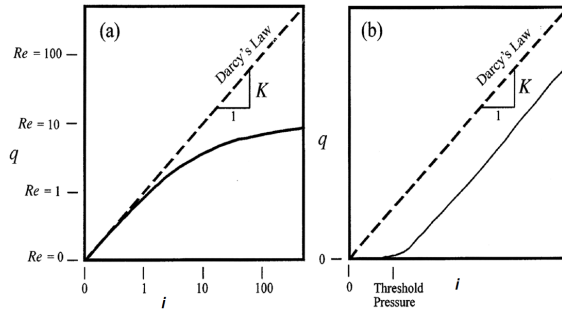


Figure 4: Upper (a) and Lower (b) borderline Situation for Darcy's Law (Hermann, 1999)

Darcy is established for steady-state flow both experimentally and theoretically [15].

2.3 Theis Solution

2.3.1 Governing Equations

The Theis solution is a process for the evaluation of aquifer tests under unsteady flow conditions. It was originally developed for confined aquifers, but it can be used for unconfined aquifers as well. In 1935, the American hydrogeologist Charles Theis set an analogy between heat flow and ground water flow resulting in the following equation [18]:

$$h_{srt} = \frac{Q}{4\pi K h_M} W(u), \quad (9)$$

with

$$u = \frac{r^2 S}{4K h_m t}. \quad (10)$$

h_{srt} = drawdown at the distance r [m]

Q = discharge [$m^3 s^{-1}$]

K = hydraulic conductivity [ms^{-1}]

h_m = groundwater thickness [m]

$W(u)$ = Theis well function [-]

r = radial distance between well and measuring point [m]

S = storativity [-]

t = time [s]

It is important to correct the drawdown for unconfined aquifers using the following equation:

$$h_{scor} = h_s - \frac{h_s^2}{2h_m}. \quad (11)$$

h_{scor} = corrected drawdown [m]

h_s = measured drawdown [m]

h_m = groundwater thickness [m]

Out of these equations transmissivity and storativity can be calculated. $W(u)$ is the Theis well function:

$$W(u) = -0,5772 - \ln(u) + u - \frac{u^2}{2 * 2!} + \frac{u^3}{3 * 3!} - \frac{u^4}{4 * 4!} + \dots \quad (12)$$

There are tables and type curves for the function for practical use in order to measure transmissivity and storativity graphical [18]. Table 9 in the appendix shows $W(u)$ values for its respective u values. Nowadays it is also quite common to use computers and special software instead of graphs on a paper.

2.3.2 Assumptions

It is necessary to make basic assumptions about the aquifer, the pumping and the observation wells in order to measure the ground water flow to wells and the sought properties of the aquifer such as transmissivity or storativity.

First the aquifer must be bounded on the bottom by a confining layer. It is seen as homogeneous and isotropic as well. All geologic formations have an infinite horizontal extent. The potentiometric surface of the aquifer is horizontal and not changing with time prior to the start of the pumping. All changes in the position of the potentiometric surface are because of the pumping well alone. The entire groundwater flow is radial to the well and horizontal in general. Furthermore, Darcy's law has to be valid. The ground water is assumed to have a constant density and viscosity as well. Moreover, the pumping well and the observation well are fully penetrating over the entire thickness of the aquifer. It has an infinitesimal diameter and a 100 percent efficiency.

In addition to the basic assumptions, Theis added the following assumptions:

1. The aquifer is confined top and bottom.
2. There is no source of recharge to the aquifer.
3. The aquifer is compressible and water is released instantaneously from the aquifer as the head is lowered.
4. The well is pumped at a constant rate.

[16]

2.4 Finite Element Method

The finite element method (FEM) is a mathematical method for solving numerical problems like field problems in science and engineering [19]. This numerical method approximates solutions of boundary value problems. A boundary value problem is a mathematical problem in which one or more dependent variables must satisfy a differential equation everywhere within a known domain of independent variables and satisfy specific conditions on the boundary of the domain. The domain of interest is called field. Dependent variables governed by the differential equation are the field variables. Depending on the type of problem being analyzed, the field variables include different physical properties such as temperature. The boundary conditions (BCs) are specific values on the boundaries of the field [20]. There are three types of BCs which are commonly used. The Dirichlet BC (also called first-type BC) specifies the value of the function itself, while the Neumann BC (second type BC) specifies the value of the normal derivative of the function [21]. The third type is the Mixed BC. It is a combination of the Dirichlet and Neumann BC. On disjoint parts of the boundary the solution of the given equation must solve either a Dirichlet or a Neumann BC [22]. All BCs are available in the DwarfElephant package.

The FEM dates back at least half a century. In 1960 the term finite element was first used by Clough [20]. FEM is supported by a rich mathematical theory with proofs about accuracy, stability, convergence and solution uniqueness [9].

A complex structure is subdivided into smaller and much simpler elements of finite dimensions called finite elements. These elements are connected at a finite number of nodes or nodal points. Depending on the structure different kind of forms are used. Figure 5 shows types of elements which are commonly used.

The discretization of a structure is called meshing (see Figure 6 for an example mesh from the MOOSE framework). The number of elements in the mesh affects the accuracy of the calculation. More elements increase the accuracy. However, more elements also mean more calculations to be done and more time needed to perform the task. Therefore, the mesh should have just enough elements to give sufficient accuracy in a reasonable compute time [23]. But with increasing performance of computers, higher amounts of data can be processed and more precise results can be produced within a reasonable time.

The finite differences method (FDM) is another technique used to obtain approximate solutions governed by differential equations. In FDM the field variable is computed at specific points only [20]. The area between these points will be approximated via difference quotients. The points are positioned in a rectangular and equidistant formation. This is why round or bent structures are difficult to discretize. As a result irregular geometries require far more effort in FDM compared to FEM [24]. A crucial disadvantage of the FDM compared to the FEM is the approximation of the area between the points. It is only valid, as long as nothing particular changes between the points. This results in a loss of quality, especially for complex problems [25]. For simple geometries on the other hand FDM produces similar results compared to FEM [24].

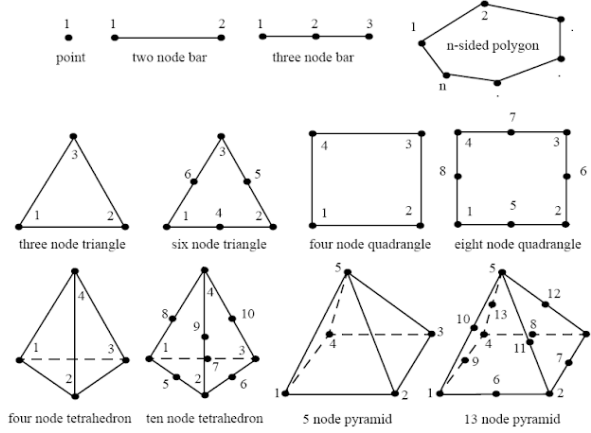


Figure 5: Different Types of Elements (habituatingfea.blogspot.com)

2.4.1 Processing

The general procedure for FE can be divided into three processing steps. The first step is preprocessing, where the model is being defined. This includes the meshing of the model and the definition of the physical constraints or boundary conditions.

In the second phase a FE software assembles the governing algebraic equations in matrix form and computes the unknown values of the field variables (it is

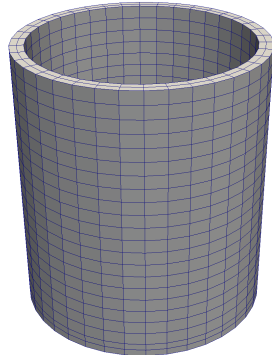


Figure 6: Mesh which represents a Mug (MOOSE.org)

also possible to assemble the equations manually). The computed values are then used (by back substitution) to compute additional, derived variables. This phase is called solution phase. The last step is postprocessing. In this step, the solutions will be analyzed and evaluated. The most important objective however is to determine whether the results are physically plausible [20]. Using FEM to find the solution to a PDE starts with forming a "weighted residual" or "variational statement" or "weak form". The idea behind generating a weak form is to give flexibility, both mathematically and numerically. A weak form is needed to input to solve a new problem [9]. Generating a weak form generally involves these steps:

1. Write down strong form of PDE.
2. Rearrange terms so that zero is on the right hand side.
3. Multiply the whole equation by a "test" function.
4. Integrate the whole equation over the domain.
5. Integrate by parts (using the divergence theorem) to get the desired derivative order on your functions and simultaneously generate boundary integrals.

2.5 Reduced Basis Method

The Reduced Basis Method is a model reduction technique. Its primary goal is the acceleration of the forward simulations. This acceleration is being achieved via a reduction of the spatial and temporal degrees of freedom. The Reduced Basis Method is only useful for simulations which must be performed in a short amount of time or very often.

The simulation processes are decomposed in an online and an offline stage. The online stage includes the fast and cheap stages of the process. This stage must always be performed.

The offline stage includes the expensive stages of the process. During the offline stage a reduced basis space will be constructed via the Greedy Algorithm, which constructs a solution space using a training set. An error Bound is obtained enabling the determination of the upper border of the loss of precision. It is only once necessary to perform the expensive offline stage. This is the reason why a high amount of computer resources is being saved resulting in a lower calculation time as well.

The advantage of time gain comes with a loss of precision in the process. As a result, there are three main questions to be asked before performing the Reduced Basis Method:

1. How big is the increase in computing time?
2. Is the necessary quality and precision still given?
3. Which steps and methods are necessary to construct a faster model?

[26][27][28]

3 Model

The simulations were performed for two different geologic formations. The first formation is a homogenous and isotropic cube representing a uniform geologic formation. The second formation consists of 3 horizontal layers representing a simple geologic sedimentary sequence without any kind of tectonic deformation, faults and so on (see Figure 7). Both examples are cubic and have a nondimensional edge length of 1. In the 3 layer model the layer boundaries are located in the nondimensional depths of 0.33 and 0.67. The unsorted mesh of both formations was built in gmsh 3.0.6 with a global mesh size factor of 0.05 with a total number of 7861 nodes.

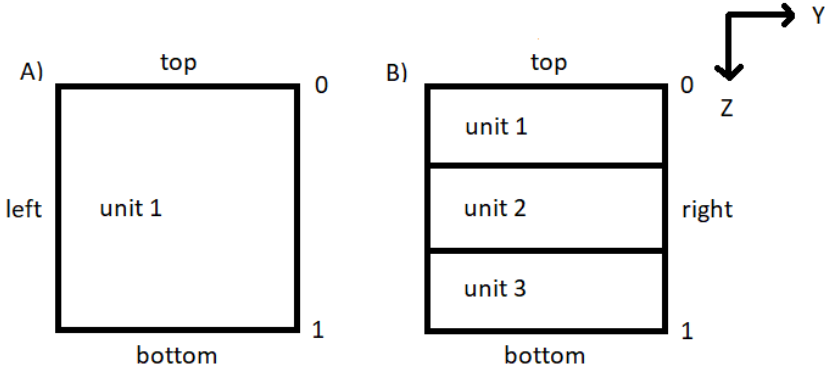


Figure 7: Sketch of the applied Model for both geologic Formations

4 Methodology

In this chapter the methodology for the Fourier and Darcy simulations is portrayed together with the programming steps for the Theis Solution.

For Fourier and Darcy, all relevant parameters are defined. The boundary conditions are set and the kind of boundary condition defined. The parameters are nondimensionalized. At last, the analytical solutions are derived for the following evaluation of the simulations both in steady and transient state.

After the execution of the simulations and the programming of the Theis Solution the results are plotted using Python and Paraview during the postprocessing for further evaluation in the following results chapter.

4.1 Fourier

For the fourier simulations, a Dirichlet boundary condition was set at the top and a Neumann boundary condition was set at the bottom of the two meshes. But before the execution of the simulation, it is necessary to define values of the temperature and the lengths of the model. The lengths are defined as 1000 m for every edge. In the 3 layer model the layer boundaries are located in a depth of 330 m and 670 m. A thermal gradient of 0.03 K/m is used. This gradient corresponds the average thermal gradient in the earth crust. For the surface of the model 10°C are defined. The calculated temperature on the bottom of the model in 1000 m depth is 40°C according to the thermal gradient. Both temperatures are necessary for the following calculation of the heat flux of the Neumann boundary condition.

These values need to be nondimensionalized in order to implement them into the simulation. The number of relevant parameters shall be reduced while characteristic parameters shall be identified and highlighted. 1000 m and 10°C are defined as reference values for the following nondimensionalization:

$$x_{non} = \frac{x}{x_{ref}} = \frac{1000m}{1000m} = 1, \quad (13)$$

$$T_D = \frac{T_1 - T_{ref}}{T_{ref}} = \frac{10^\circ C - 10^\circ C}{10^\circ C} = 0, \quad (14)$$

$$q_N = \frac{\frac{T_1 - T_{ref}}{T_{ref}} + \frac{T_0 - T_{ref}}{T_{ref}}}{\frac{x}{x_{ref}}} = \frac{\frac{40^\circ C - 10^\circ C}{10^\circ C} + \frac{10^\circ C - 10^\circ C}{10^\circ C}}{\frac{1000m}{1000m}} = \frac{3 - 0}{1} = 3. \quad (15)$$

T_{ref} = reference temperature [-]

T_1 = surface temperature [°C]

T_0 = bottom temperature [°C]

T_D = Dirichlet temperature [-]

q_N = Neumann flux [-]

x_{non} = nondimensionalized length [m]

x = length [m]

x_{ref} = reference length [m]

It is also necessary to nondimensionalise the thermal conductivity k using the following equation:

$$k_{non} = \frac{k}{k_{ref}} \quad (16)$$

k_{non} = nondimensionalized conductivity [-]

k = thermal conductivity [$Wm^{-1}K^{-1}$]

k_{ref} = reference conductivity [$Wm^{-1}K^{-1}$]

The reference conductivity is set as 1.

The analytical solution for the steady state simulation is derived using the Fourier Law:

$$q = -k \frac{dT}{dz} = -k \frac{T_{m+1} - T_m}{z_{m+1} - z_m} \quad (17)$$

The equation gets rearranged after T_{m+1} :

$$T_{m+1} = -\frac{q}{k}(z_{m+1} - z_m) + T_m \quad (18)$$

T_m = temperature on different depths m [-]

q = heat flux [-]

k = thermal conductivity [-]

The boundary conditions define the initial temperature T_0 and the heat flux q . The Dirichlet boundary condition provides T_0 as the initial temperature which was previously defined as zero. The Neumann boundary condition provides the flux q . $z_m = 0$ is the starting point on the top of the model. The flux q is constant because of the steady state condition. The power in Watt is defined by energy per unit of time. The energy however must be constant in this case because the entire process does not depend on time. As a result, the flux (which is defined as power per area) has to be constant in every point as well. This is why the Neumann flux can be used for the calculation in every point. The minus in the equation has to be removed to show the calculated temperatures according to the model in geologic coordinates.

The final solution of the analytical steady state case is:

$$T_{m+1} = \frac{q_N}{k}(z_{m+1} - z_m) + T_m \quad (19)$$

T_m = temperature on different depths m [-]

q_N = Neumann flux [-]

k = thermal conductivity [-]

The analytical solution for the transient simulation gets derived from the Heat Conduction Equation. It is a partial differential equation of the form:

$$\frac{\delta U}{\delta t} = \alpha \frac{\delta^2 U}{\delta x^2} \quad (20)$$

U = temperature [-]

t = time [-]

α = thermal diffusivity [-]

[29]

The inserted values get previously nondimensionalized. The thermal diffusivity α can be calculated using the following equation:

$$\alpha = \frac{k}{\rho c_p} \quad (21)$$

k = thermal conductivity [$Wm^{-1}K^{-1}$]

ρ = density [kgm^{-3}]

c_p = specific heat capacity [$Jkg^{-1}k^{-1}$]

[30]

The density and the specific heat capacity are predefined as 1 in the simulation. This is why the thermal diffusivity α can be replaced by the thermal conductivity k .

From the Heat Conduction Equation, Weisstein, Eric W. derived a solution for calculating the temperatures U depending on the time t and the distance x [29]:

$$U(x, t) = \frac{1}{2}c_0 + \sum_{n=1}^{\infty} c_n \cos\left(\frac{n\pi x}{L}\right) e^{-k\left(\frac{n\pi}{L}\right)^2 t} \quad (22)$$

where

$$c_n = \frac{2}{L} \int_L^0 \cos\left(\frac{m\pi x}{L}\right) U(x, 0) dx \quad (23)$$

L = total length [-]

t = time [-]

k = thermal conductivity [-]

$U(x, 0)$ = initial condition [-]

m = integer [-]

c_0 and c_n can be determined using the boundary conditions. However, this solution is only valid when the Neumann boundary condition is replaced by a Dirichlet boundary condition.

4.2 Darcy

For Darcy, a Dirichlet and a Mixed boundary condition was set. The penalty factor of the Mixed boundary condition is 100000. The penalty factor defines, whether a Mixed boundary condition is more like a Dirichlet or a Neumann boundary condition. A high penalty factor shifts it towards the Dirichlet boundary condition. In this case, the high penalty factor shifts it into a nearly pure Dirichlet boundary condition. A horizontal groundwater flow parallel to the layering was simulated. Therefore, the boundary conditions are not set on the top and bottom of the mesh, but on its left and right side.

Just like in the Fourier simulation, variables such as the pressure and lengths as well as constants such as the permeability need to be nondimensionalized. The nondimensionalization of the length is the same as for Fourier's law:

$$y_{non} = \frac{y}{y_{ref}} = \frac{1000m}{1000m} = 1, \quad (24)$$

y_{non} = nondimensionalized length [−]

y = length [m]

y_{ref} = reference length [m]

For the nondimensionalization of the permeability, it is necessary to predefine a reference permeability and the real permeabilities of the aquifer for every single layer. The reference permeability is defined as 10^{-12} . The real permeabilities are defined as 10^{-12} for the upper and lower layer. The middle layer has a permeability of 10^{-10} . This layer represents a layer with preferred groundwater flow.

$$k_{non} = \frac{k}{k_{ref}} \quad (25)$$

k_{non} = nondimensionalized permeability [−]

k = permeability [m^2]

k_{ref} = reference permeability [m^2]

As a result, the nondimensionalized permeability of the upper and lower layer is 1 and in the middle layer 100.

It is also necessary to nondimensionalise the dynamic viscosity μ .

$$\mu_{non} = \frac{\mu}{\mu_{ref}} \quad (26)$$

μ_{non} = nondimensionalized viscosity [−]

μ = viscosity [$m^2 s^{-1}$]

μ_{ref} = reference viscosity [$m^2 s^{-1}$]

The reference viscosity is set as 1 as well as the real viscosity. As a result, the nondimensionalized viscosity is 1.

The pressure is nondimensionalized using the following equation:

$$p_{non} = \frac{p_y - p_0 + \rho g z}{y_{ref}}. \quad (27)$$

p_{non} = nondimensionalized pressure [-]

p = pressure [pa]

p_0 = atmospheric pressure [pa]

ρ = fluid density [kg/m^3]

g = gravitation constant [m/s^2]

z = depth [m]

y_{ref} = reference length [m]

On both boundaries, the depth for every point is defined as 0, in order to remove the hydrostatical component. As a result, only p_y is relevant for the calculation of the pressures on the boundaries. p_y can also be written as:

$$p_y = \rho g H + p_0, \quad (28)$$

where H is the Hydraulic Head above the reference height. It becomes clear that the Hydraulic Head is the crucial factor for changing the pressure. For the left side, a head of 20 m was defined and for the right side a head of 0 m. The pressure is shown in meter of water and not Pascal. The calculated boundary conditions are:

$$p_{mixed} = \frac{20m}{1000m} = 0.02, \quad (29)$$

and

$$p_D = \frac{0m}{1000m} = 0. \quad (30)$$

p_D = pressure on the dirichlet boundary [-]

p_{mixed} = pressure on the mixed boundary [-]

The analytical solution for the steady state simulation is derived using the Darcy equation:

$$u = -\frac{k}{\mu} \frac{dp}{dy} = -\frac{k}{\mu} \frac{p_{m+1} - p_m}{y_{m+1} - y_m} \quad (31)$$

The equation is rearranged after p_{m+1}

$$p_{m+1} = -\frac{u\mu}{k} (y_{m+1} - y_m) + p_m \quad (32)$$

p_m = pressure on different distances m [-]

u = float rate per unit area [-]

k = permeability [-]

y_m = distances m [-]

The Mixed boundary condition defines the initial value p_0 as 0.02 which was previously calculated.

The analytical solution for the transient simulation is similar to the analytical solution from the Heat Conduction Equation. It is only necessary to replace the thermal conductivity with $\frac{k}{\mu}$ and U with p:

$$\frac{\delta p}{\delta t} = \frac{k}{\mu} \frac{\delta^2 p}{\delta x^2} \quad (33)$$

p = pressure [-]

t = time [-]

k = hydraulic permeability [-]

μ = dynamic viscosity [-]

4.3 Theis Solution

The Theis Solution was programmed using Python. Its code can be found in the appendix. The code was designed to show the drawdown in a confined predefined aquifer in a radial distance to the pumping well. It is possible to show multiple time steps as well as only one time step at once. The radial distance and the time range can be chosen freely.

The governing equations of chapter 2.3 for u , $W(u)$ and h_{srt} were implemented. In order to save computing power, it was examined after which part of the convergent series of $W(u)$ a breakup can be done without losing quality. A break up after the sixth part keeps the required precision even for higher u values.

Before the implementation of the equations, it is necessary to predefine multiple variables such as the production rate, storativity, transmissivity, hydraulic conductivity and the groundwater filled aquifer thickness. After that, a vector for the radial distances was implemented followed by the time steps and the governing equations. The drawdown and radial distance are nondimensionalised by dividing them by the groundwater filled aquifer thickness.

5 Results

5.1 Fourier

The analytical values for the homogeneous and 3 layer steady state simulations are shown in Table 2 and 3. In this chapter however only the plots of the 3 layer simulation are discussed because the results of the 3 layer simulation already show every information necessary for the further discussion and conclusion. The plots of the homogeneous steady state simulation can be found in the appendix.

Table 2: Values of the Analytical homogeneous Fourier steady State Solution

Layer	k [-]	Thickness [-]	Depth [-]	Temperature [-]
Layer 1	2.0	1.0	1.0	1.50

Table 3: Values of the Analytical 3 layer Fourier steady State Solution

Layer	k [-]	Thickness [-]	Depth [-]	Temperature [-]
Layer 1	2.3	0.33	0.33	0.4304
Layer 2	1.0	0.34	0.67	1.4504
Layer 3	2.3	0.33	1.0	1.8809

The curves of FE, RB as well as the analytical curve confirm the anticipations based on the derived analytical equation in the previous chapter. They are being built by 'straight lines', which change slope by reaching another layer with a different thermal conductivity. A higher thermal conductivity results in a lower slope. This observation is discussed in the following chapter. The values of both FE and RB show little to no differences to the analytical solutions. It is also not possible to see any difference between the RB and FE data in Fig.8. The combined plot shown in Fig.9 does not give any hints of major differences between FE, RB and the analytical solutions. But in FE and RB there are noticeable 'gaps' between the layer boundaries and the boundary surfaces which can be observed in both previously mentioned figures. In these gaps, no values from the simulations are plotted leaving the space near the the layer boundaries and the boundary surfaces empty.

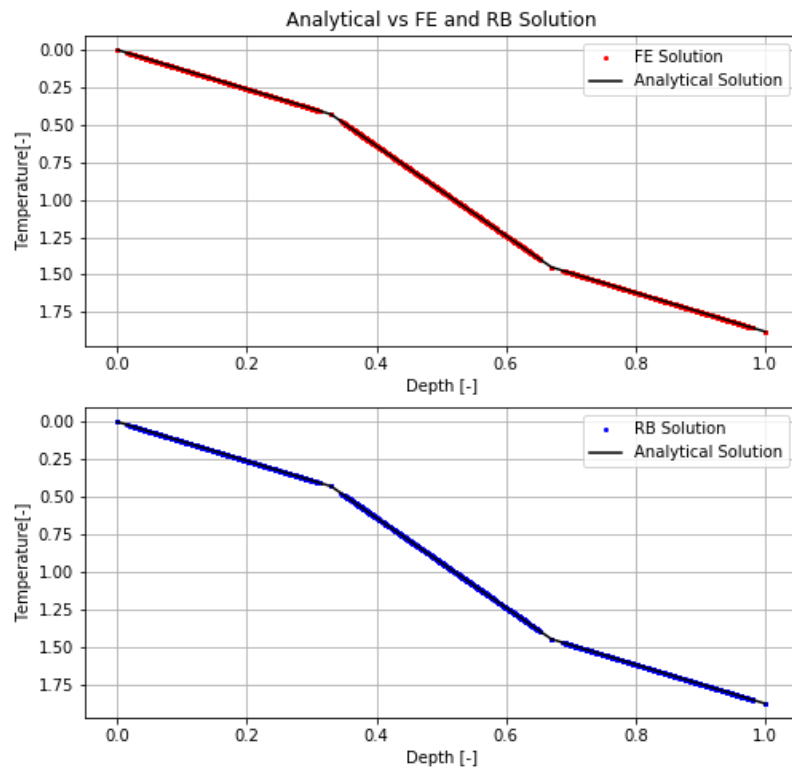


Figure 8: Fourier Plot of the FE and RB Node Values plotted against the Depth (seperated)

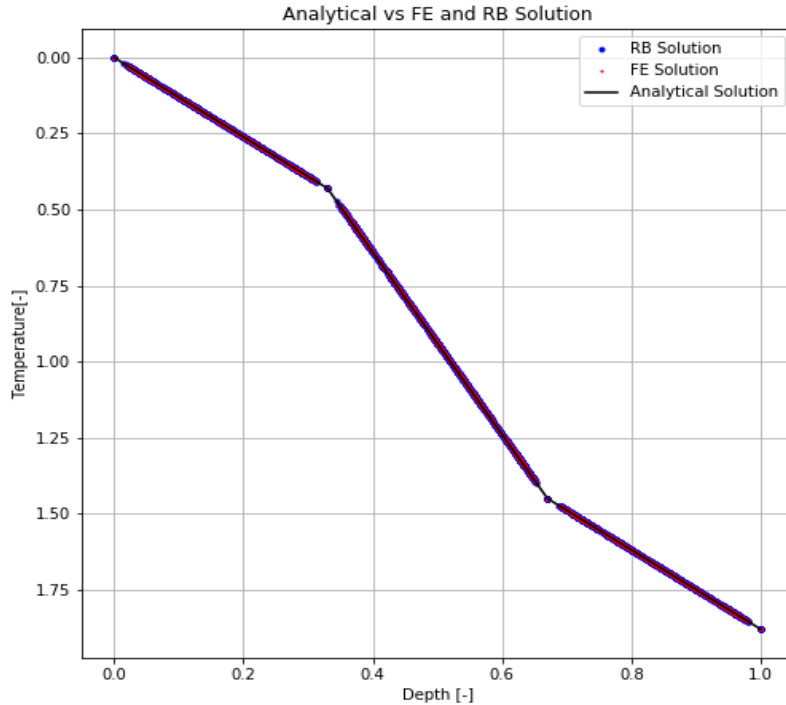


Figure 9: Fourier Plot of the FE and RB Node Values plotted against the Depth (combined)

The three dimensional difference plots of the FE and RB datasets in Fig.10 and 11 reveal an increasing error with increasing depth along the z-axis. Furthermore, a region with a higher positive and a region with a higher negative error can be observed. Moreover, the biggest errors appear to be found on the boundaries of the mesh. The error on the boundaries is in a range between 10^{-8} and -10^{-10} which can be considered as very small.

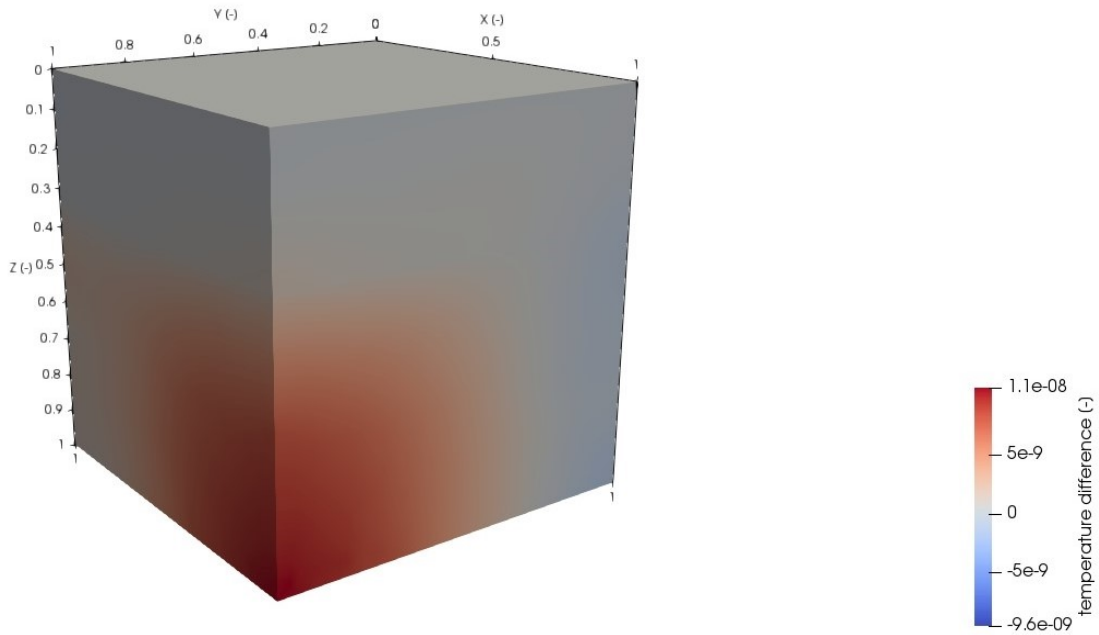


Figure 10: Difference Plot shown from the side with the highest positive Temperature Difference between FE and RB

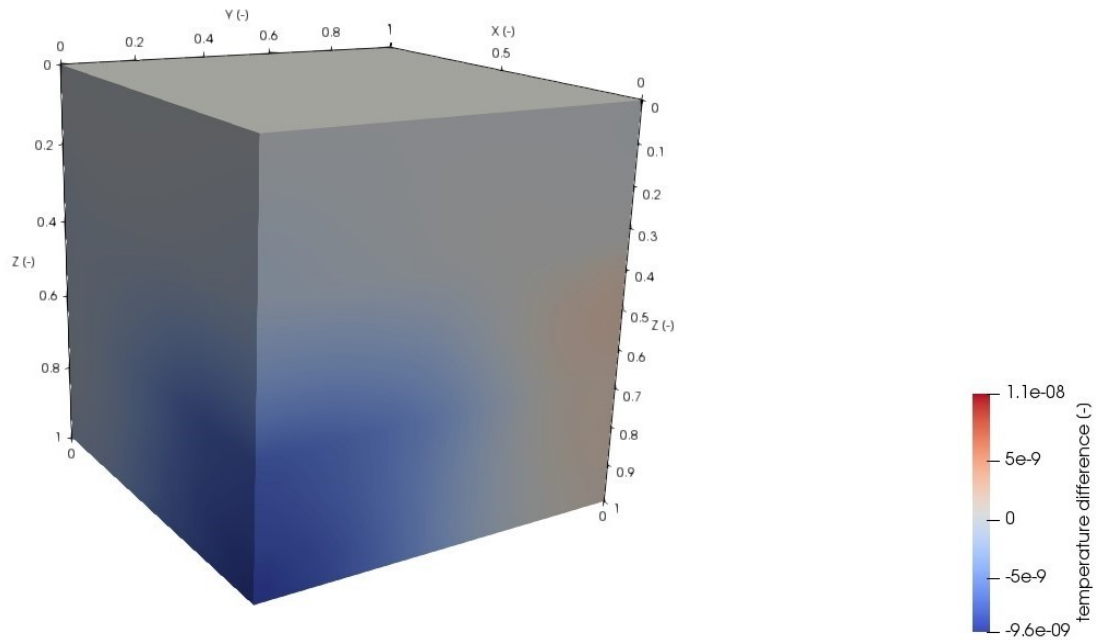


Figure 11: Difference Plot shown from the side with the highest negative Temperature Difference between FE and RB (displayed by 180 Degree compared to Fig.10)

Fig.12 shows the difference plot where the upper 100 m (or 0.1 nondimensional lenght units) of the 3 surfaces in the field of view were sliced down. The relative errors on the inside are not higher compared to the surfaces errors. A second slicing operation for the remaining 3 sides (which is not shown here) show the exact same results.

The slices confirm this observation concerning the maximum errors. None of the slices along all of the three axis in Fig. 13, 14 and 15 show a higher errors inside the mesh. The slices normal to the x- and y-axis and parallel to its remaining axes confirm an increasing error in higher depths as well as regions with higher positive and negative errors (also confirmed with the mesh normal to the z-axis).

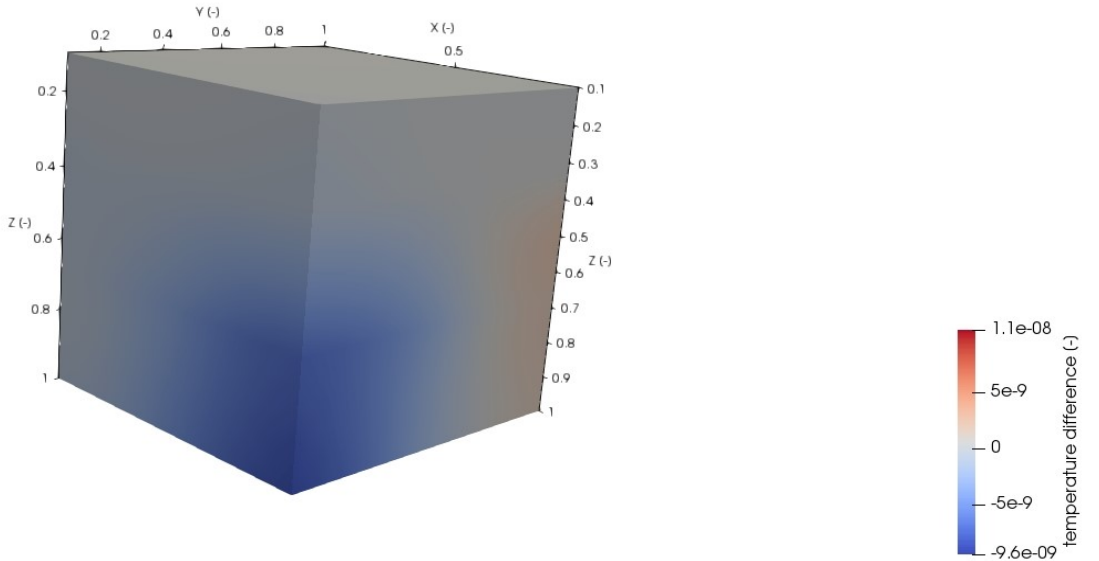


Figure 12: Steady State Fourier Difference Plot, upper Regions of the Surfaces sliced down

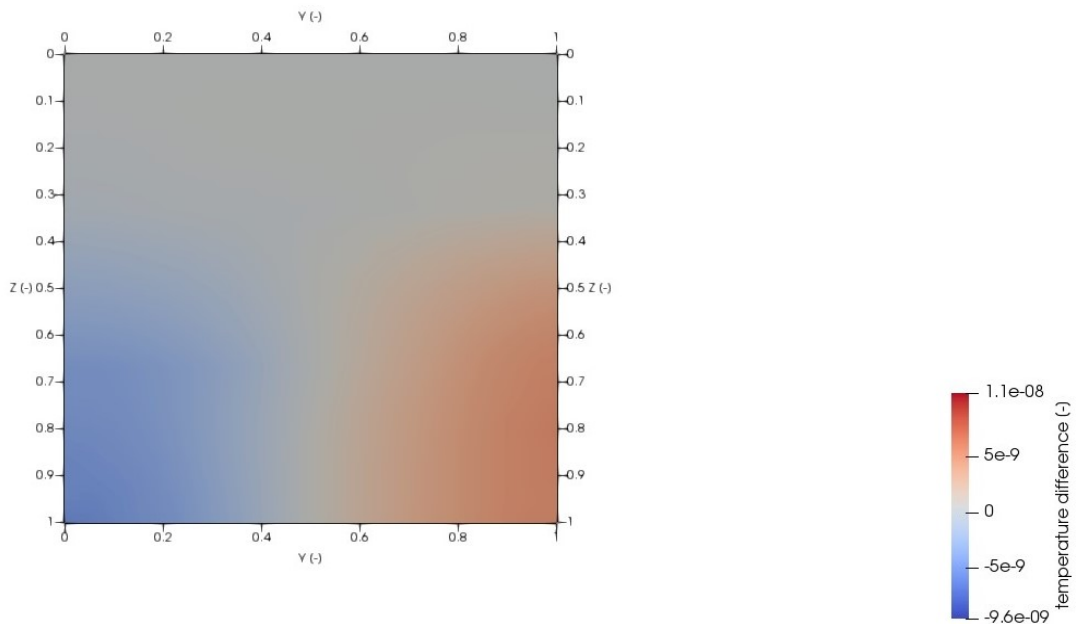


Figure 13: Slice normal to the x-axis on the steady Fourier Simulation

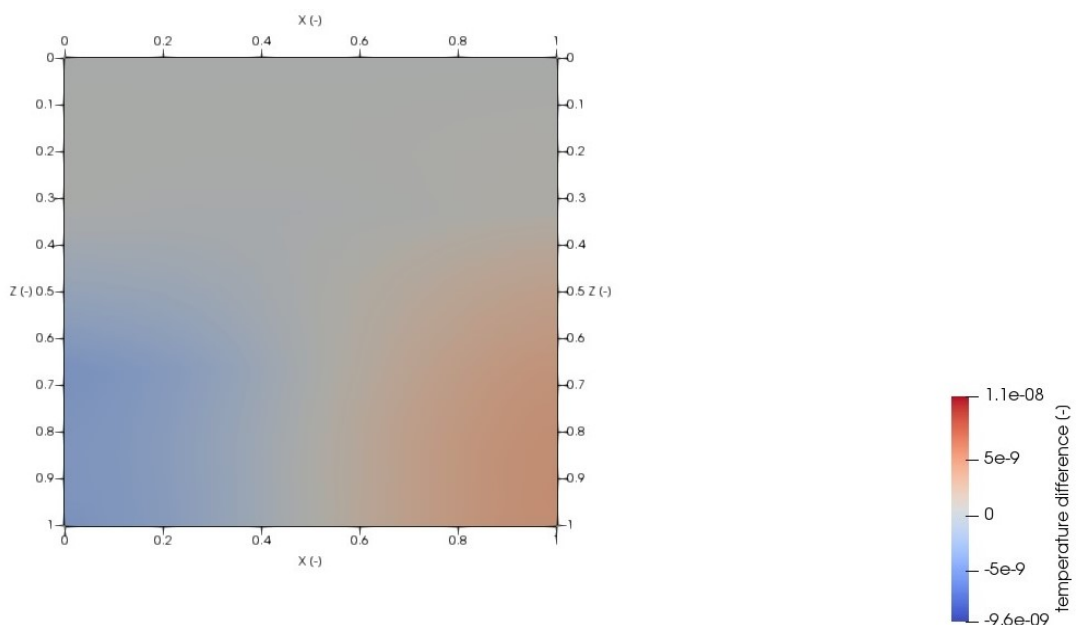


Figure 14: Slice normal to the y-axis on the steady Fourier Simulation

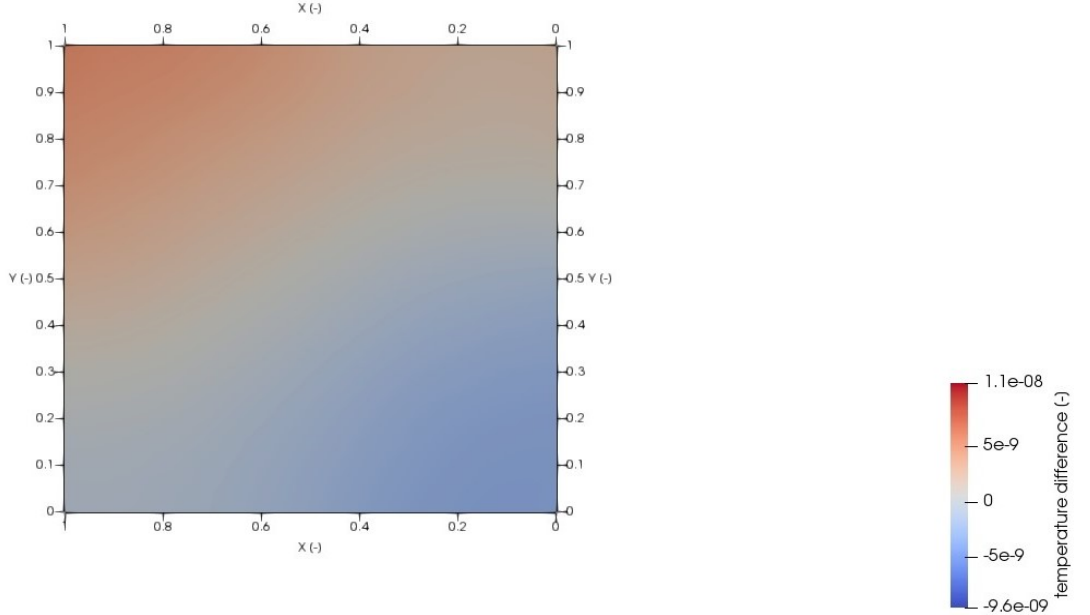


Figure 15: Slice normal to the z-axis on the steady Fourier Simulation

The transient simulation shows an overall increase of temperature between the boundaries during the time steps. A comparison between Fig.16 and 17 shows this process. Furthermore, the process passes over from a transient to a steady state case with time. The course of temperature changes not only by time but also by the different layers. In Fig.18 the temperature curves of the two time steps in Fig. 16 and 17 are plotted. There the change of temperature distribution can be observed better. It becomes clear that both previous observations are confirmed. In the last timestep ($dt = 1.6$) the steady state case is practically reached. The only reason its curve does not match the curves from Fig.8 and 9 is the change of the Neumann boundary condition into a Dirichlet boundary condition. Furthermore, in the first shown timestep the plot shows an uneven and slightly curvy form while the second plotted later timestep consists of straight lines (see Fig.18).

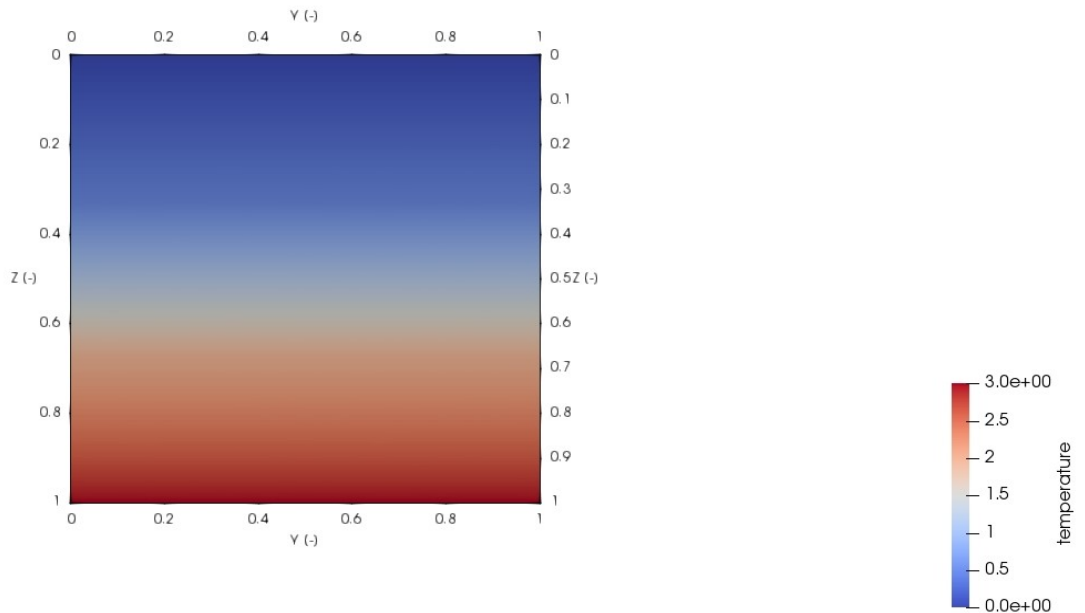


Figure 16: Transient Fourier Temperature Plot ($dt = 0.2$), Temperature in [-]

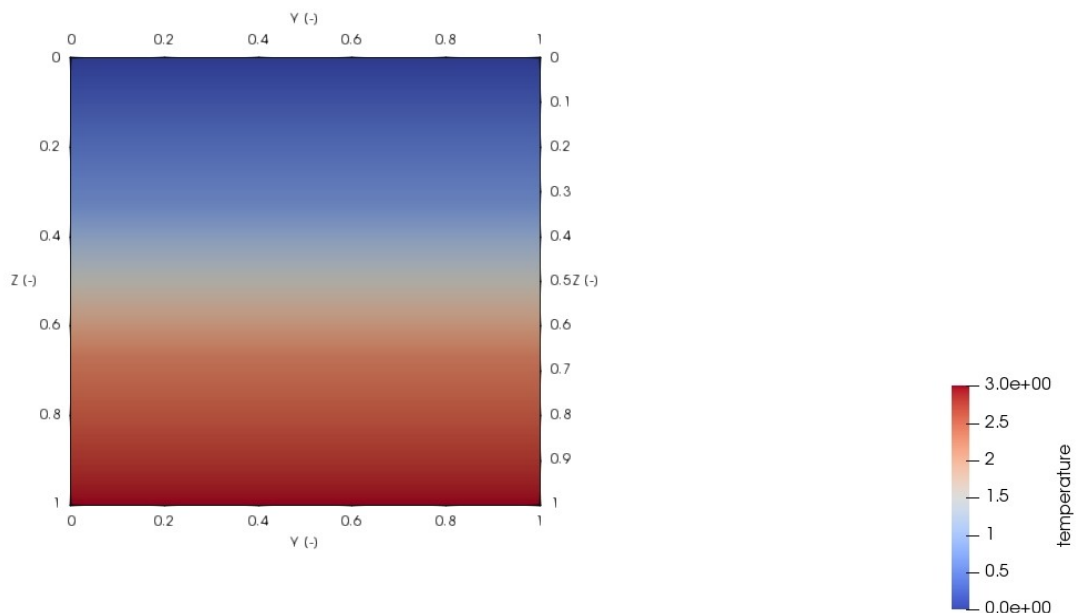


Figure 17: Transient Fourier Temperature Plot ($dt = 1.6$), Temperature in [-]

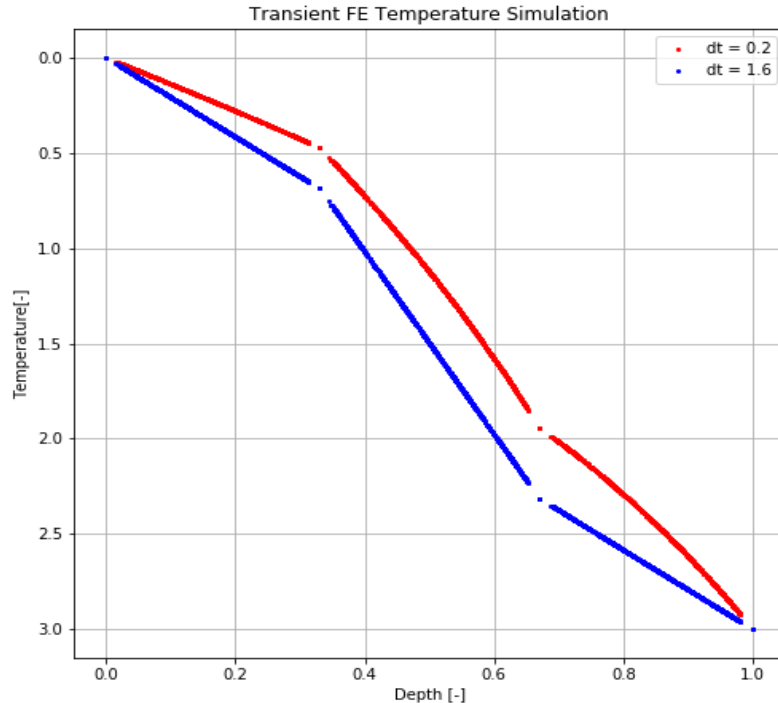


Figure 18: Plot of the transient FE Temperature simulation, first and last timestep are shown

5.2 Darcy

The analytical values for the homogeneous and 3 layer steady state simulations are shown in Table 4 and 5. Just like in the previous chapter only the plots of the 3 layer simulation are discussed for the same reasons. However, the plots of the homogeneous steady state simulation can also be found in the appendix.

Table 4: Values of the Analytical steady state homogeneous Darcy Solution

Layer	k [-]	Thickness [-]	Distance [-]	Pressure [-]
Layer 1	1.0	0.33	1.0	0.0

Table 5: Values of the Analytical steady state 3 layer Darcy Solution

Layer	k [-]	Thickness [-]	Distance [-]	Pressure [-]
Layer 1	1.0	0.33	1.0	0.0
Layer 2	100.0	0.34	1.0	0.0
Layer 3	1.0	0.33	1.0	0.0

The values of the simulation are identical to the analytical solution as shown in Fig.19. Just like in the Fourier simulations, it is not possible to see any differences between the FE and RB solution in Fig.19 and 20. This time however, the values build a straight line without any changing slopes. Furthermore, the curves of the homogeneous and the 3 layer simulation are the same as can be seen in the analytical solutions. The 'gaps' near the boundaries of the mesh can again be observed like in the Fourier simulation.

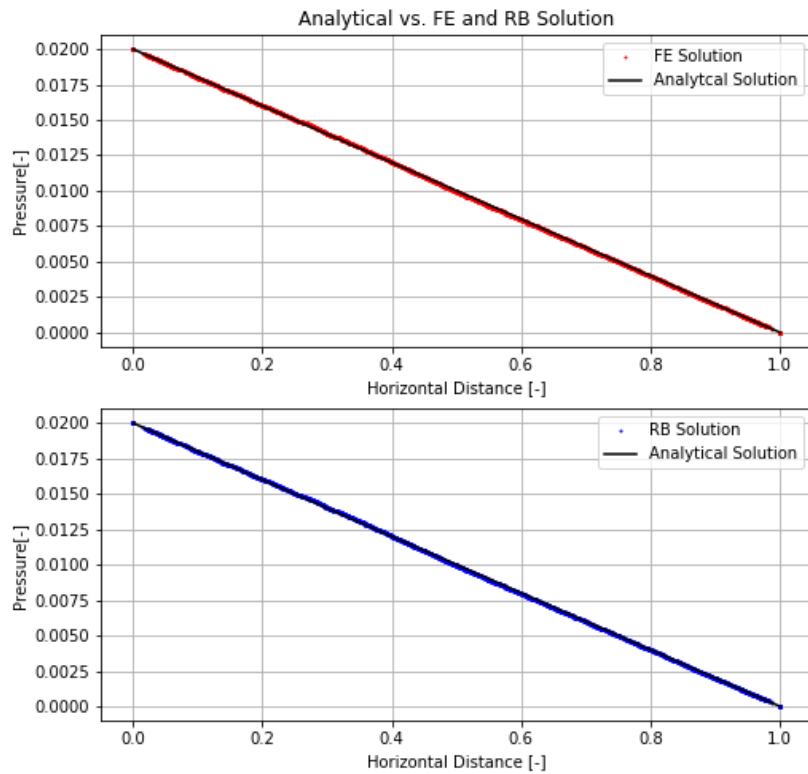


Figure 19: Darcy Plot of the FE and RB Node Values plotted against the Depth (separated)

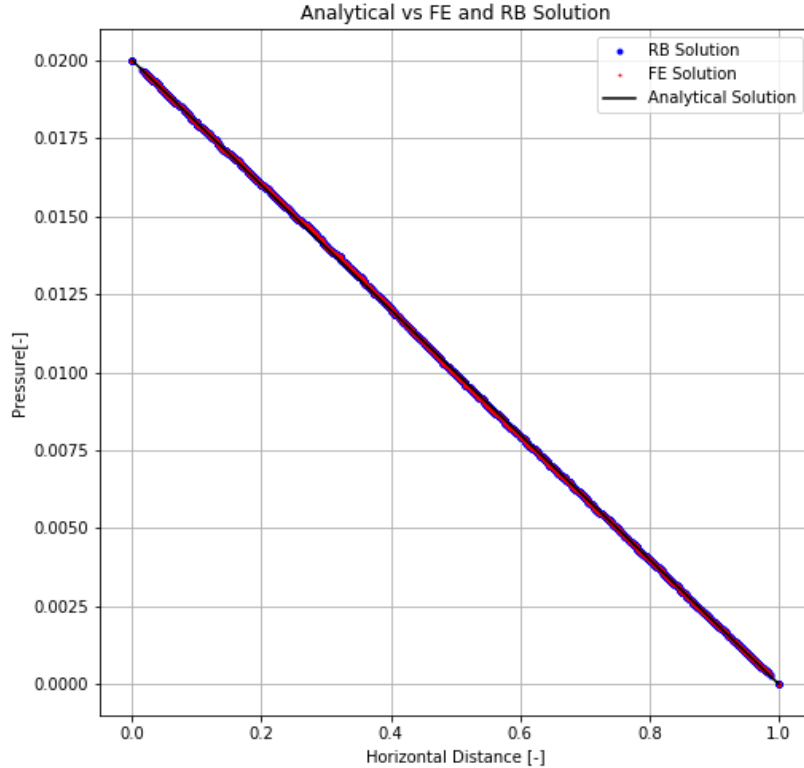


Figure 20: Darcy Plot of the FE and RB Node Values plotted against the Depth (summarised)

The three dimensional difference plot for the 3 layer case shown in Fig.21 and 22 show a significantly higher error on the left boundary of the model compared to the remaining parts. The errors especially at the layer boundaries are significantly increased. From the left to the right side, a shift of the error between RB and FE can be seen from negative along the y-axis until an error of exactly zero is reached on the right side where the Dirichlet boundary condition is set (see Fig.21 and 22). There is also a high error contrast between the different layers on the left side making the layering visible which can also be seen in Fig 21. The error ranges from $5.1 * 10^{-7}$ to $-2.5 * 10^{-6}$.

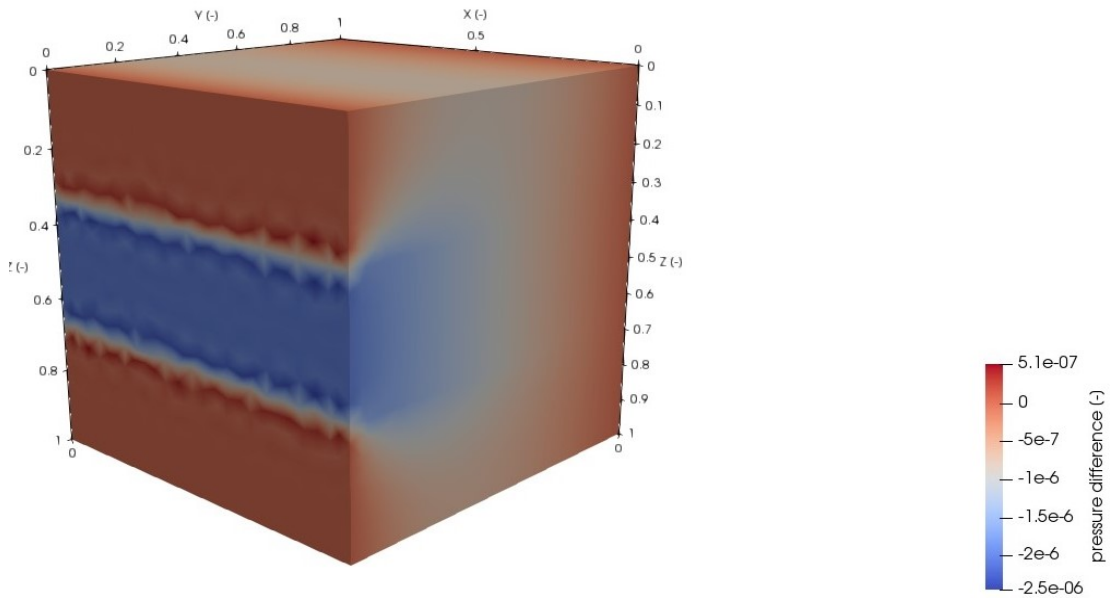


Figure 21: Darcy steady state Pressure Difference Plot shown from the left Side in Front

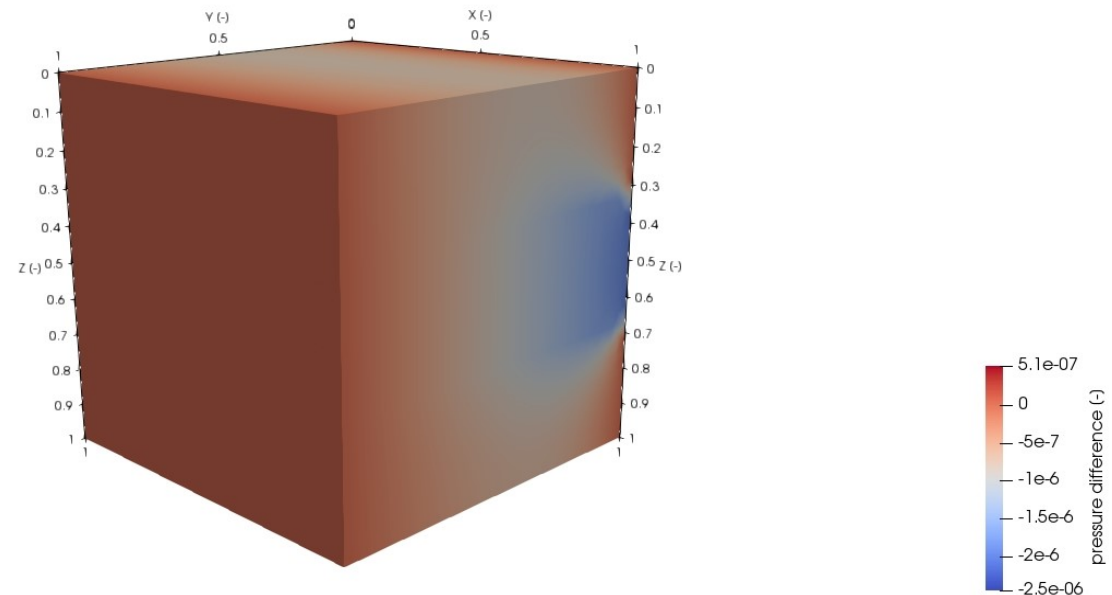


Figure 22: Darcy steady state Pressure Difference Plot shown from the right Side in Front

Similar to Fig.12 in the Fourier simulation Fig.23 shows a difference plot where the upper 100 m (or 0.1 nondimensional length units) of the 3 surfaces in the field of view were sliced down. The relative errors on the inside are not higher compared to the surfaces errors. Thus, the results are similar to the Fourier simulation concerning the comparison between the errors on the boundaries and below them.

Slices through the model also show that the biggest errors are once again located on the boundaries of the mesh just like in Fouriers case as the following Figures 24, 25 and 26 show. In Fig.24, the error contrast between the middle and the outer layers becomes visible as well. In Fig.26, where the slice normal to the z-axis is shown, the shift is even more visible. The change to increasingly positive errors here is visible as well. The slice normal to the y-axis and parallel to the other two axis is right in the middle of the cube (Fig.25). There the relative errors are very homogeneous.

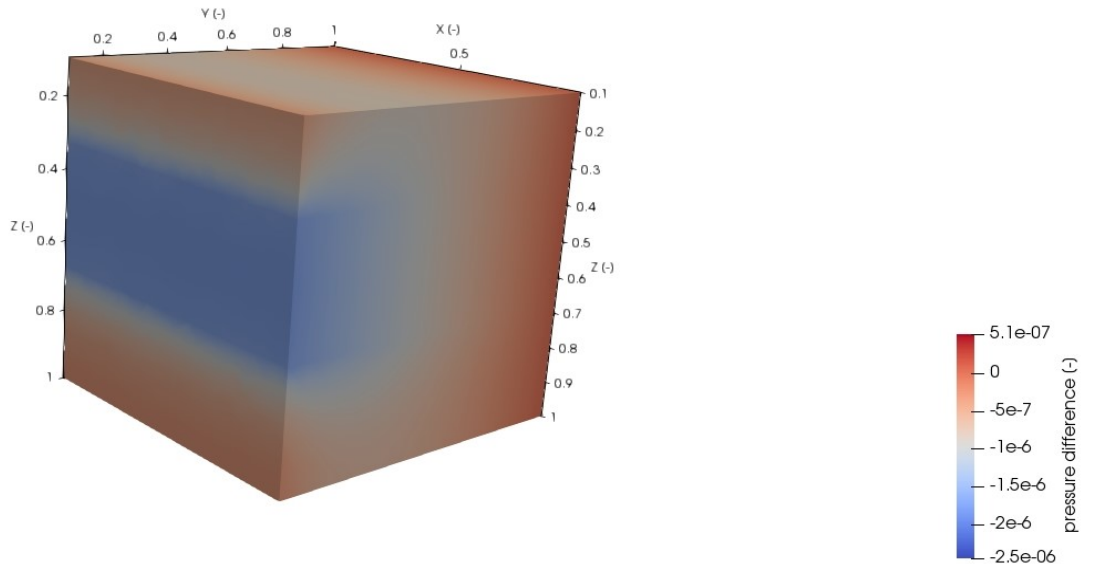


Figure 23: Steady State Darcy Difference Plot, upper Regions of the Surfaces sliced down, left side in Front

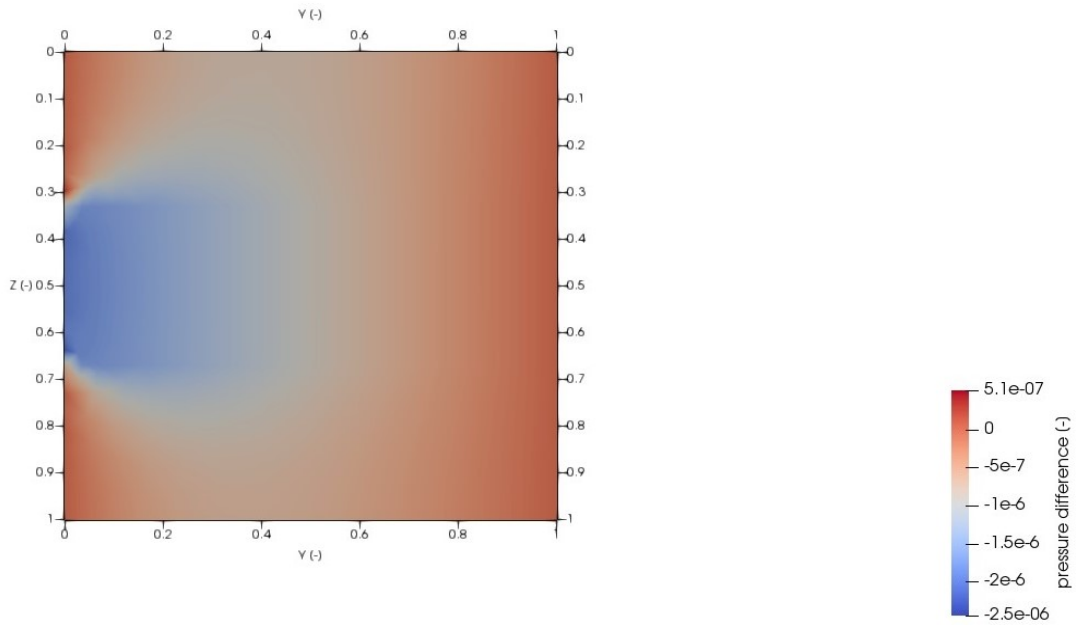


Figure 24: Slice normal to the x-axis on the steady Darcy Simulation

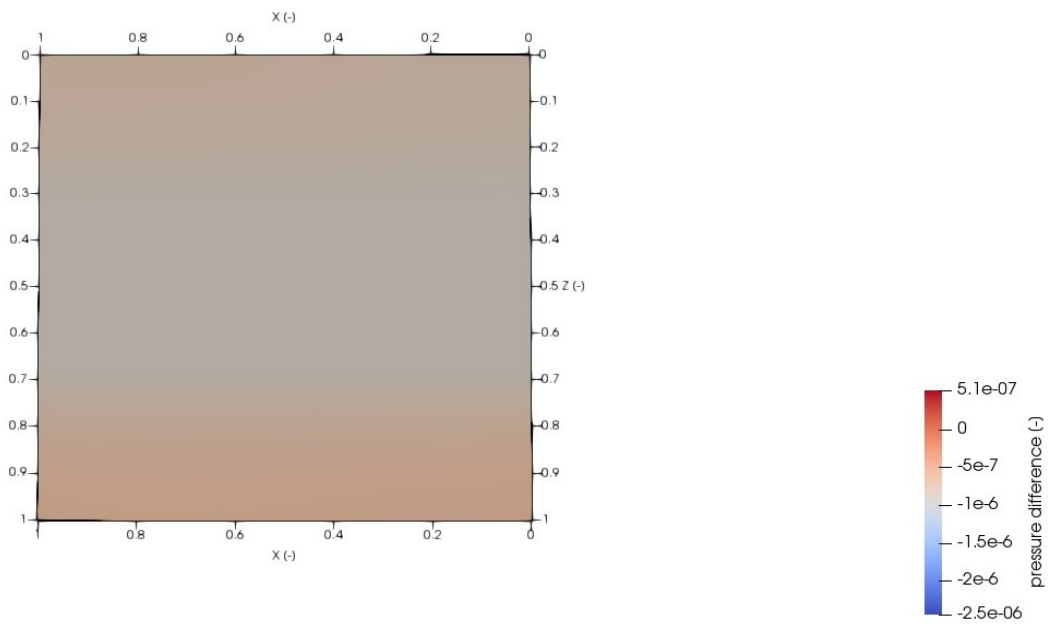


Figure 25: Slice normal to the y-axis on the steady Darcy Simulation

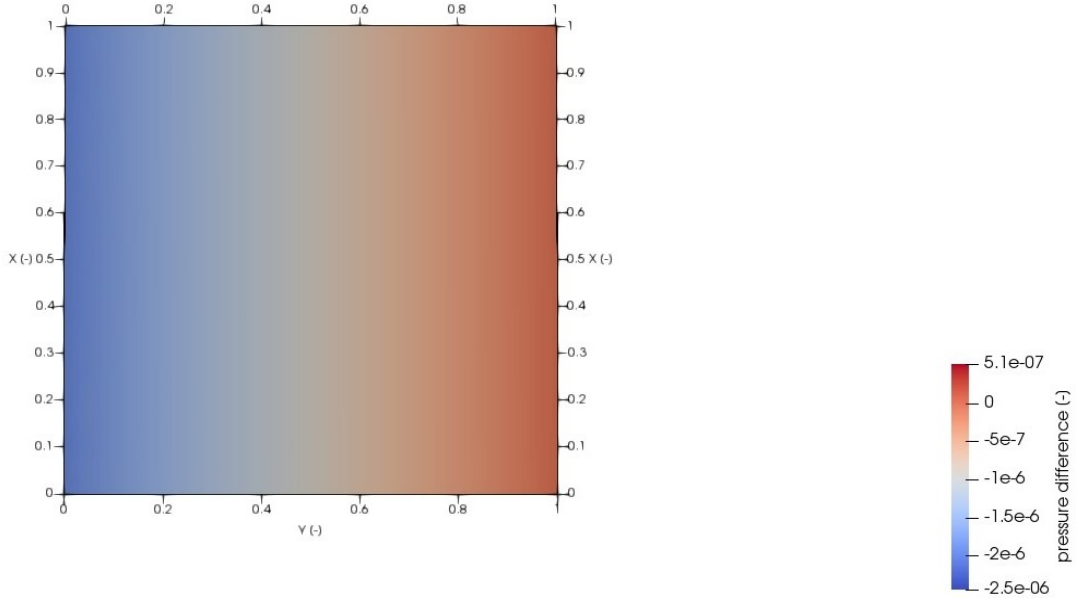
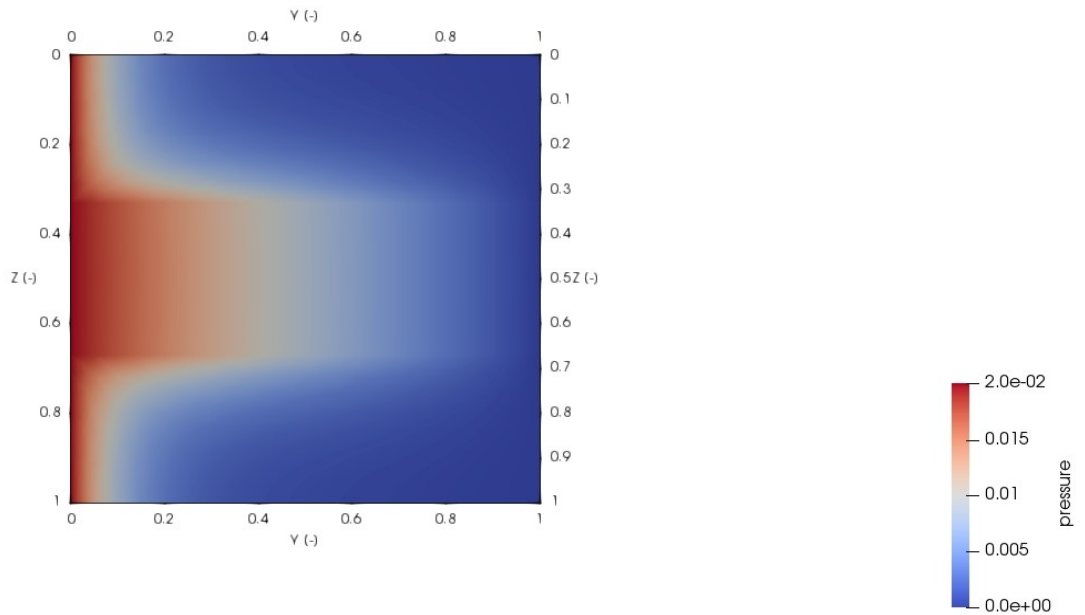
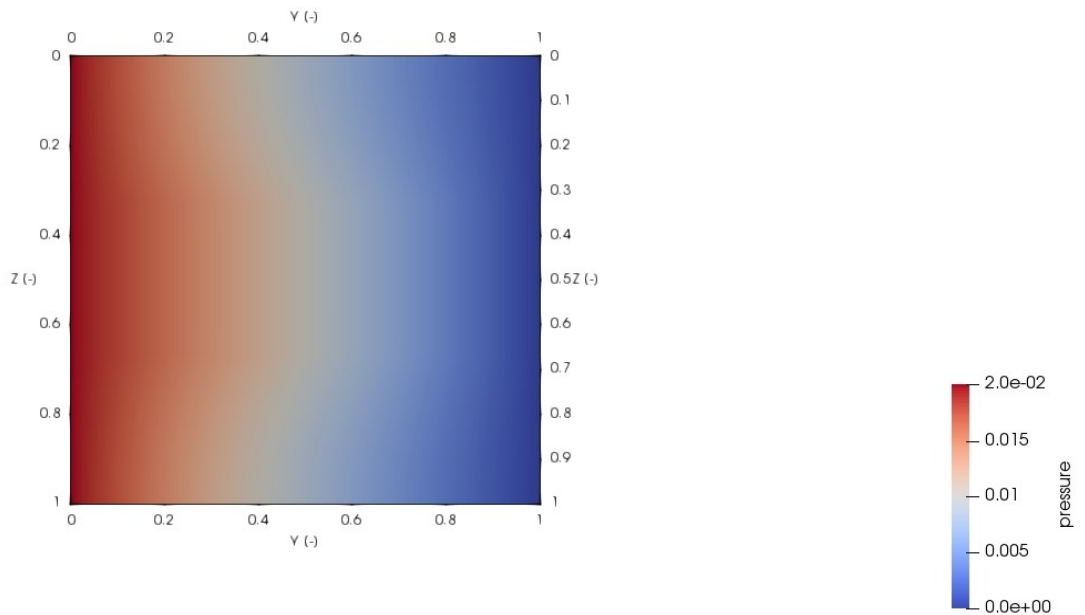


Figure 26: Slice normal to the z-axis on the steady Darcy Simulation

In the transient simulation, the initial pressure distribution is not equal in every layer. Layers with a higher hydraulic permeability have a higher pressure. The pressure difference becomes smaller by the following time steps which can be observed in Fig.27 and 28. The transient state converts into a steady state case by the time. This behaviour is similar to the Fourier Simulation. Fig.29 shows the steady state solution of the previous simulation plotted with the transient solutions of two different time steps. There the transformation from the transient to the steady state can be clearly seen. In $dt = 0.1$ the steady state is almost completely reached.

Figure 27: Transient Darcy Pressure Plot ($dt = 0.01$), Pressure in [-]Figure 28: Transient Darcy Pressure Plot ($dt = 0.1$), Pressure in [-]

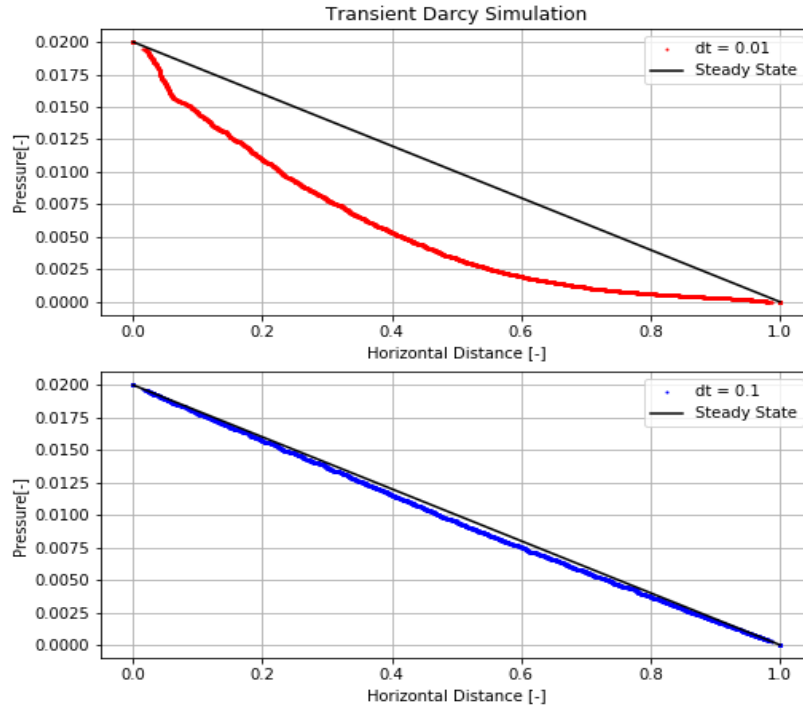


Figure 29: Plot of the transient FE Darcy Simulation, first and last Timestep are shown

5.3 Theis Solution

The plot in Fig.30 shows the drawdown of a predefined aquifer after 5 different timesteps. The used aquifer parameters are shown in Table 6.

The code was validated in every implemented function and the resulting drawdowns. The calculation of the variable u was performed in the Python script as well as manually. The results of the script match perfectly to the manual solutions. The auxillary function $W(u)$ was validated by calculating its solutions for different u values. The solutions of the script were compared to the values in Table 9 which can be found in the appendix. The values from the script match to the values in the table, as Table 7 shows. These values however are already rounded to the second decimal, which means that there is already a minor error between both values. The Theis solution itself however has already errors bigger than that due to the necessary factor of hydraulic conductivity or transmissivity whose measurement has already a high error tolerance due to the natural inhomogeneous traits of a natural aquifer. This is why it can easily be said that the calculated values for $W(u)$ are sufficient in their precision.

The last step of the validation of the script is the plot of manually calculated drawdown values into its curve calculated by the Python script. Both calcula-

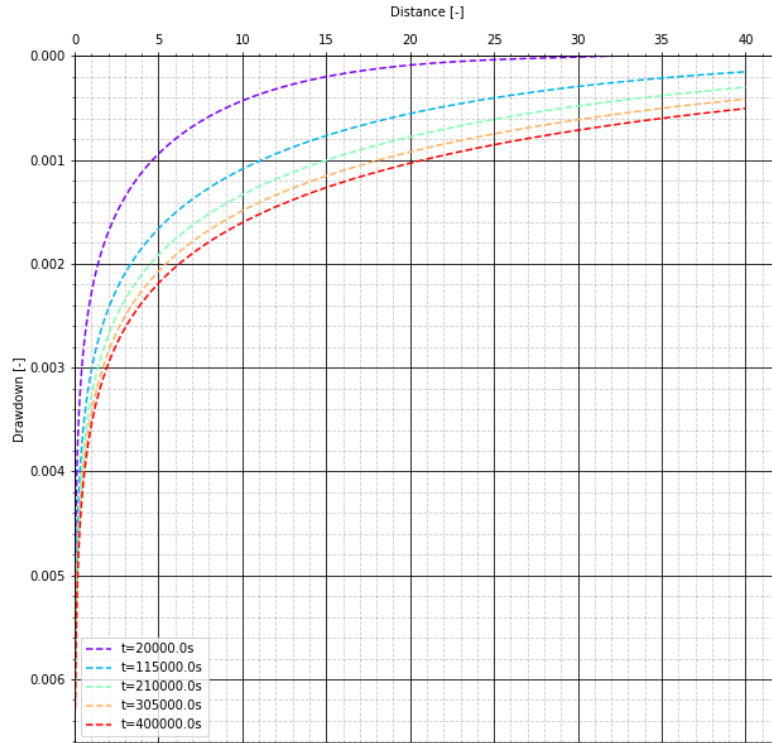


Figure 30: Drawdown Curves for a predefined Aquifer mady by the Python Script

tions were made using the parameters in Table 6. Table 8 shows the resulting drawdowns in certain radial distances.

Fig. 31 shows that the analytical solutions and the curve made by the Python script perfectly match. Major differences are not visible.

Table 6: Predefined Aquifer Parameters used for the Validation of the Theis Solution

Parameter	Value
Q	$0.002 \text{ m}^3/\text{s}$
S	0.005
K	$6 * 10^{-4} \text{ m/s}$
h_m	25m
t	360000s

Table 7: $W(u)$ Values calculated by the Python Script vs. $W(u)$ Values from Literature) for certain u Values

u	$W(u)$ (Python Code)	$W(u)$ (Table 9)
10^{-10}	22.4487	22.45
10^{-9}	20.1461	20.15
10^{-8}	17.8435	17.84
10^{-7}	15.5409	15.54
10^{-6}	13.2383	13.24
10^{-5}	10.9357	10.94
10^{-4}	8.6332	8.63
10^{-3}	6.3316	6.33
10^{-2}	4.0379	4.04
10^{-1}	1.8229	1.823

Table 8: Manually calculated Radial Distances and the respective Drawdowns

Number	Radial Distance [m]	Drawdown [m]
1	50	0.0730
2	150	0.0500
3	250	0.0390
4	500	0.0247
5	1000	0.0117

6 Discussion

The values of the simulations match the analytical solutions. No major differences can be found for both FE and RB. As a result, the simulations are successfull concerning the overall outcome.

More importantly, the range of difference between FE and RB are very small. The error tolerance is set at 10^{-5} . The relative error of the steady Fourier Simulation varies in a range between 10^{-8} and 10^{-10} while the relative error of the steady Darcy Simulation varies in a range between 10^{-6} and 10^{-7} . That means that the error of the steady Darcy Simulation is up to 100 times higher compared to the steady Fourier Simulation. The reason behind the higher error in the 3 layer Darcy simulation lies in the inserted parameters. The homogeneous Darcy simulation (see Fig.36) has much lower errors in the range of 10^{-8} . The only difference between the homogeneous and the 3 layer Darcy simulation is the 100 times higher permeability in the middle of the 3 layer model. As a result, higher contrasts result in a higher error in the RB simulation. The homogeneous and 3 layer Fourier simulations on the other hand do not show higher error differences because the difference between the thermal conductivities is much smaller than in the Darcy simulations (2.3 vs. 1 compared to 100.0 vs. 1). Nonetheless, even the highest errors in the Darcy Simulation are still 10 times smaller as the accepted error tolerance. Furthermore, the highest errors are only found on the surface with the Mixed boundary condition near the layer boundaries while the remaining areas show much smaller errors. Even though the strongly increased errors are only local between the layer boundaries, even higher permeability contrasts may result into even higher errors that can get

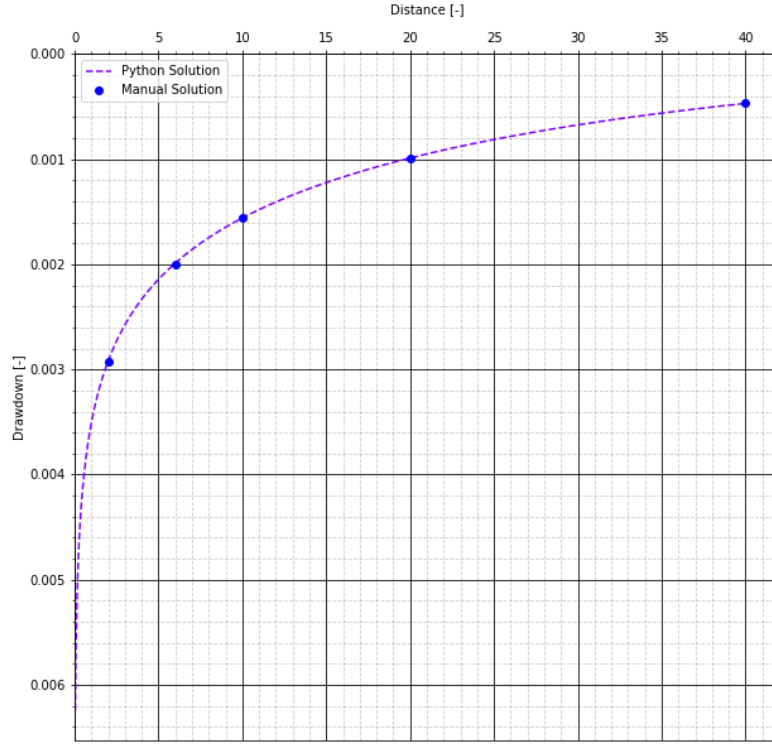


Figure 31: Plot of a Drawdown Curve calculated by Python and manually calculated Solutions

close to the error tolerance but this is only limited to a minor part of the model. The largest part of the model however would still be below the error range even with higher contrasts.

More importantly, the spatial variation of the errors depends on the set boundary conditions. The error on the Dirichlet boundary conditions is always zero which can be seen in the previous chapter. The reason of the absence of errors comes from the character of the Dirichlet boundary itself. There a value of a function itself is defined. As a result, no calculation is performed which means no errors due to calculations can arise. On the Neumann and Mixed boundary conditions on the other hand, calculations have to be performed. Therefore a reduction must be performed with a maximal tolerated error range inevitably resulting in errors in the calculation. This is the reason why the areas with the highest errors in the simulation are always positioned near the Neumann or Mixed boundary condition. The 'gaps' that are mentioned in the previous chapter do not result from the boundary conditions. The reason behind these gaps is the applied mesh. The mesh is unstructured. There is no variation in the

direction normal to the surfaces near layer boundaries. This lack of variation results in a space where no nodes are positioned. That is the reason why the plots in the previous chapter show these 'gaps'.

Another observed phenomenon is the change of slope in the Fourier Simulations for steady and transient state. The reason behind the changing slopes a layer boundaries is the changing thermal conductivity of the respective layers. A higher thermal conductivity results into a lower slope while a lower thermal conductivity results into a higher slope. When a material has a higher thermal conductivity, the heat can be transported faster through the layer which leads into a lower temperature difference between the top and the bottom of a layer. A lower thermal conductivity on the other hand leads to a higher temperature difference due to its relatively poor heat transportation which causes the higher slope seen in the results.

In the steady Darcy Simulations the homogeneous and the 3 layer solutions show no differences in their curves although there is a difference in the permeabilities. A very important aspect for explaining the observed solution is the proportionality between u and k . The pressure gradient in the steady state is constant. The u value must also be constant under a constant pressure gradient. Besides, the law of conservation of mass must be valid. As a result, the flow u must be constant in every single area of the model including the boundaries. An increase of the permeability results into an increase of u . It is apparent in the following switched Darcy equation, that proportional increases of u have no effect on the pressure gradient. As a result the higher permeability of the middle layer in the 3 layer model does not change the distribution of pressure and as a consequence, the results of the homogeneous and 3 layer model are equal.

$$-\frac{u\mu}{k} = \frac{dp}{dx}. \quad (34)$$

u = float rate per unit area [ms^{-1}]

k = hydraulic permeability [m^2]

μ = dynamic viscosity of the fluid [$m^2 s^{-1}$]

p = pressure [pa]

In the transient Darcy Simulation however, the permeability affects the pressure distribution. The layer with a higher permeability shows higher pressure compared to its neighbouring low permeable layers. There is a preferential flow in the high permeable layer. As a result, the hydraulic head increases. This effect becoming visible through a higher pressure. By the time, the system changes into a steady state system with similar characteristics to the previously calculated steady state Simulations. This transformation into a steady state system is physically explainable. Every imbalanced system tries to reach balance which can be found in the steady state.

In the transient Fourier Simulation, a slower progress in the spread of temperature can be observed for the middle layer. The reason behind this observation is the lower thermal conductivity of the layer. The transformation of the transient state into steady state follows the same principle like in the transient Darcy

Simulation.

The programmed code for the Theis Solution shows results which are in accord to the manually calculated values. The drawdown increases with time and decreases with increasing radial distance to the pumping well. Every governing equation implemented in the code is validated as correct. Altogether, the programmed code is capable of calculating the correct drawdowns dependent on radial distance, time, the aquifer properties and the pumping conditions. The real drawback of the code is its limited range of use. It is only possible to simulate the drawdown if every relevant parameter is known or predefined. In real pumping tests however, aquifer properties such as the transmissivity and storativity should mostly be identified. This is not possible with this code. For the measurement of these properties it is still necessary to use the type curve method.

7 Conclusion

Based on the discussed results of the steady and transient state simulations, the FE and RB implementation deliver both correct solutions. None of the calculated simulation data vary from the analytical solution in both the temperature and pressure benchmarks.

The maximum relative error range of 10^{-5} was not reached both in the Fourier and the Darcy Simulations. As a result, the RB implementation does not exceed the maximum range of tolerance. In conclusion it is proven that the RB implementation of the DwarfElephant package matches the required precision. It can definitely be said that the validation of the DwarfElephant package on the basis of diffusion controlled pressure and temperature benchmarks was successful. The package can be used for its original purpose.

The results of the programmed Python code for the Theis Solution deliver correct solutions. Every implemented governing equation was validated as correct. As a result, the Python code can be used as a basis for an implementation into DwarfElephant using C++ instead of Python.

8 Outlook

As a last step for the validation of the package, a comparison between the transient FE and RB values will be necessary. The process is similar to the applied methods of this thesis.

Based on the previous results of the benchmarking process for Fouriers and Darcys law, other geoscientific problems can be implemented as well using the DwarfElephant package. One of the possibilities would be the Theis Solution which was already described in Chapter 2.3. A Theis implementation could be used to simulate the drawdown of a confined or unconfined aquifer. This excludes the type curve method for the measurement of transmissivity and storativity. As a consequence, it will be necessary to predefine every variable in the auxillary well function as well as the drawdown function itself. Because Theis was designed for unstationary drawdown, the simulation can only be performed in the transient way. Furthermore, Theis is an empirical designed formula unlike Fouriers and Darcys law. This is why it is necessary to predefine the limitation

of the range of values, especially for the time and the variable u. The setting of boundary conditions are necessary as well. It might be useful to set the same boundary conditions like in the Darcy Simulations. For the side, where the pumping well is deployed, a Mixed boundary condition can be implemented with the value of the maximal aquifer thickness. Nondimensionalised it would mean:

$$h_{BC} = \frac{h_{srt0}}{h_m} = \frac{h_{max}}{h_{ref}} = 1, \quad (35)$$

h_{BC} = nondimensionalized drawdown [-]

h_{srt0} = drawdown in r_0 [m]

h_{max} = maximal drawdown [m]

h_m = groundwater filled aquifer thickness [m]

h_{ref} = reference height [m]

The opposite side which has the maximal distance to the pumping well is a Dirichlet boundary condition with the value zero. The mesh geometry must be adapted as well. Real aquifers have a much higher horizontal extent compared to its thickness. This is why a mesh with the form of a plate would be more useful than a cubic mesh. The mesh has to have homogeneous traits as well in order to represent an ideal homogeneous aquifer. After the implementation of the Theis Solution, other hydrogeological methods can be implemented as well such as the Cooper Jacob method. Another possible step can be the addition of the Theis type curves for further uses such as the calculation of the transmissivity and storativity.

9 References

- [1] Dale and Cory Janssen. Computer simulation. <https://www.techopedia.com/definition/17060/computer-simulation> (retrieved: 11.09.2018).
- [2] Ignacio Garcia-Dorado, Daniel G. Aliaga, Saiprasanth Bhalachandran, Paul Schmid, and Dev Niyogi. Fast weather simulation for inverse procedural design of 3d urban models. *ACM Trans. Graph.*, 36:21:1–21:19, 2017.
- [3] Magda Fontana. Computer simulations, mathematics and economics. *International Review of Economics*, 53(1):96–123, Mar 2006.
- [4] Michael St. Pierre. *Simulation in der Medizin*. Springer-Verlag GmbH, 2018.
- [5] Yaozhong Zhang, An Zhang, Qingjun Xia, and Fengjuan Guo. Research on modeling and simulation of an adaptive combat agent infrastructure for network centric warfare. In Kang Li, Minrui Fei, Li Jia, and George W. Irwin, editors, *Life System Modeling and Intelligent Computing*, pages 205–212, Berlin, Heidelberg, 2010. Springer Berlin Heidelberg.
- [6] Romain Sibois and Ali Muhammad. *State of the art in modelling and simulation*. Research Report. VTT Technical Research Centre of Finland, Finland, 2015. Project code: 100553.
- [7] S Mustafiz and Md. Robiul Islam. State-of-the-art petroleum reservoir simulation. *Petroleum Science and Technology*, 26:1303–1329, 06 2008.
- [8] Michael O’Sullivan, Karsten Pruess, and Marcelo J. Lippmann. State of the art geothermal reservoir simulation. *Geothermics*, 30:395–429, 11 2000.
- [9] MOOSE Framework Internet Page. Finite element principles. online: <http://mooseframework.org/wiki/MooseTraining/FEM/Principles/> (retrieved 11.8.2018).
- [10] Gerald Schubert Donald Turcotte. *Geodynamics*. CAMBRIDGE UNIV PR, third edition, 2014.
- [11] Christoph Clauser. *Geothermal Energy*, volume 3, chapter 8, pages 493–604. Springer Verlag, 2006.
- [12] Christoph Clauser. *THERMAL STORAGE AND TRANSPORT PROPERTIES OF ROCKS, II: THERMAL CONDUCTIVITY AND DIFFUSIVITY*, chapter 2, pages 1431–1448. K. Gupta, 2011.
- [13] Christoph Clauser. Heat transport processes in the earth’s crust. *Surveys in Geophysics*, 2009.
- [14] Stephen Whitaker. Flow in porous media i: A theoretical derivation of darcy’s law. *Transport in Porous Media*, 1(1):3–25, Mar 1986.
- [15] Ghislain De Marsily. *Quantitative Hydrogeology: Groundwater Hydrology for Engineers*. Academic Press, 1986.

- [16] C.W. Fetter Jr. *Applied Hydrogeology (4th Edition)*. Pearson, 2000.
- [17] LEXIKON DER GEOWISSENSCHAFTEN. Porengeschwindigkeit. <https://www.spektrum.de/lexikon/geowissenschaften/porengeschwindigkeit/12585> (retrieved: 02.09.2018), 2000.
- [18] Wilhelm Coldewey Bernward Höltig. *Hydrogeologie*. Spektrum-Akademischer Vlg, 2012.
- [19] LEXIKON DER GEOWISSENSCHAFTEN. Finite-elemente-methode. <https://www.spektrum.de/lexikon/geowissenschaften/finite-elemente-methode/4832> (retrieved 20.08.2018), 2000.
- [20] David V. Hutton. *Fundamentals of Finite Element Analysis*. McGraw-Hill, 2004.
- [21] A. Cheng and D. T. Cheng. Heritage and early history of the boundary element method. *Engineering Analysis with Boundary Elements*, Volume 29, Issue 3, Pages 268-302, 2005.
- [22] Martin Hermann. *Numerik gewöhnlicher Differentialgleichungen*. Oldenbourg Wissensch.Vlg, 2004.
- [23] Atlas Computer Laboratory. Finite elements (instructive movie). online: <https://www.youtube.com/watch?v=lrpj3cZrKn4> (retrieved 8.8.1018), 1975.
- [24] Autodesk.Help. Finite element vs finite volume. <https://knowledge.autodesk.com/support/cfd/learn-explore/caas/CloudHelp/cloudhelp/2014/ENU/SimCFD/files/GUID-12A9AED8-2047-4D3A-BC80-82BE9CF47517.htm.html> (retrieved: 20.08.2018), 2015.
- [25] Dr. Rolf Rannacher et. al. Finite elemente: die ideen. <https://www.spektrum.de/magazin/finite-elemente-die-ideen/823715> (retrieved: 20.08.2018), 1997.
- [26] Jan S. Hesthaven, Gianluigi Rozza, and Benjamin Stamm. *Certified Reduced Basis Methods for Parametrized Partial Differential Equations*. Springer International Publishing, 2016.
- [27] Karen Veroy, Christophe Prud'Homme, Dimitrios V. Rovas, and Anthony T. Patera. A Posteriori Error Bounds for Reduced-Basis Approximation of Parametrized Noncoercive and Nonlinear Elliptic Partial Differential Equations. In *16th AIAA Computational Fluid Dynamics Conference*, Orlando, United States, 2003.
- [28] Christophe Prud'Homme, Dimitrios V. Rovas, Karen Veroy, Luc Machiels, Yvon Maday, Anthony T. Patera, and Gabriel Turinici. Reliable Real-Time Solution of Parametrized Partial Differential Equations: Reduced-Basis Output Bound Methods. *Journal of Fluids Engineering*, 124(1):70–80, November 2001.

9 REFERENCES

- [29] Eric W. Weisstein. Heat conduction equation. From MathWorld—A Wolfram Web Resource. <http://mathworld.wolfram.com/HeatConductionEquation.html> (retrieved: 01.09.2018).
- [30] David R. Lide. *CRC Handbook of Chemistry and Physics, 90th Edition (CRC Handbook of Chemistry & Physics)*. CRC Press, 2009.

A Additional Contents

A.1 Theis W(u) Table

Table 9: W(u) Values for different u Values (Rüde, 2015)

u	$W(u)$	u	$W(u)$	u	$W(u)$	u	$W(u)$
1×10^{-10}	22.45	7×10^{-8}	15.90	4×10^{-5}	9.55	1×10^{-2}	4.04
2	21.76	8	15.76	5	9.33	2	3.35
3	21.35	9	15.65	6	9.14	3	2.96
4	21.06	1×10^{-7}	15.54	7	8.99	4	2.68
5	20.84	2	14.85	8	8.86	5	2.47
6	20.66	3	14.44	9	8.74	6	2.30
7	20.50	4	14.15	1×10^{-4}	8.63	7	2.15
8	20.37	5	13.93	2	7.94	8	2.03
9	20.25	6	13.75	3	7.53	9	1.92
1×10^{-9}	20.15	7	13.60	4	7.25	1×10^{-1}	1.823
2	19.45	8	13.46	5	7.02	2	1.223
3	19.05	9	13.34	6	6.84	3	0.906
4	18.76	1×10^{-6}	13.24	7	6.69	4	0.702
5	18.54	2	12.55	8	6.55	5	0.560
6	18.35	3	12.14	9	6.44	6	0.454
7	18.20	4	11.85	1×10^{-3}	6.33	7	0.374
8	18.07	5	11.63	2	5.64	8	0.311
9	17.95	6	11.45	3	5.23	9	0.260
1×10^{-8}	17.84	7	11.29	4	4.95	1×10^0	0.219
2	17.15	8	11.16	5	4.73	2	0.049
3	16.74	9	11.04	6	4.54	3	0.013
4	16.46	1×10^{-5}	10.94	7	4.39	4	0.004
5	16.23	2	10.24	8	4.26	5	0.001
6	16.05	3	9.84	9	4.14		

A.2 Homogeneous steady state Plots

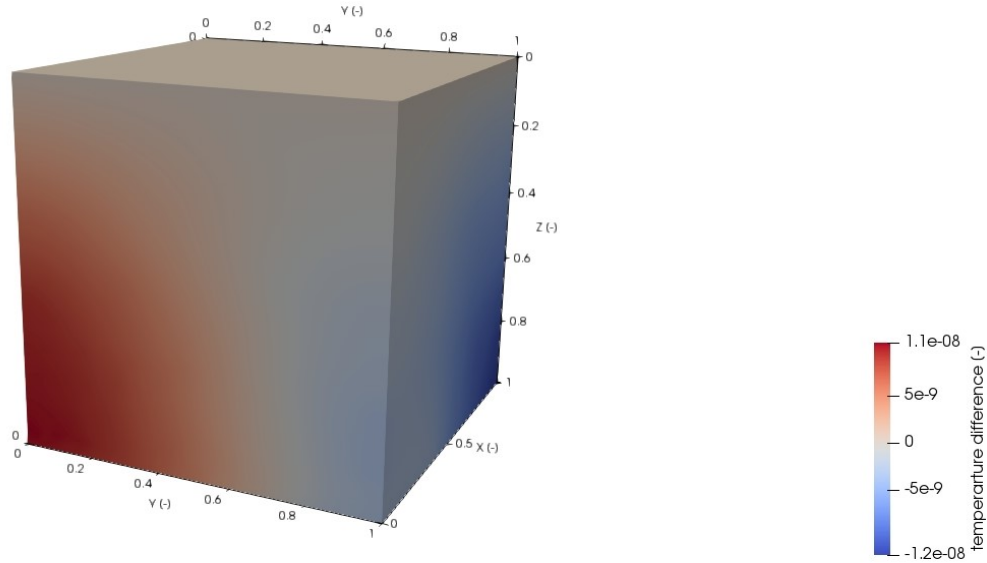


Figure 32: Steady State Fourier Difference Plot for the homogeneous Simulation

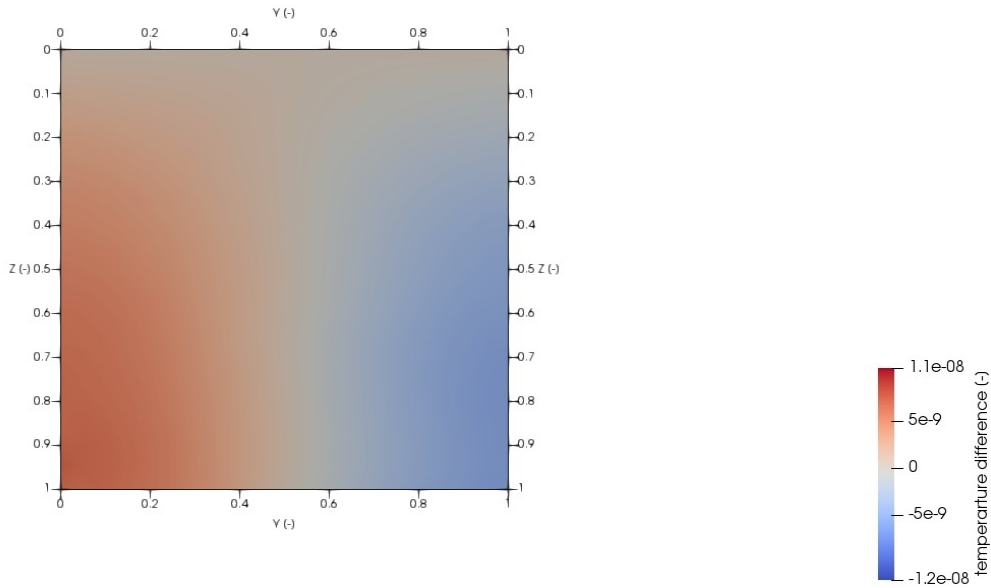


Figure 33: Slice normal to the x-axis on the homogeneous steady Fourier Simulation

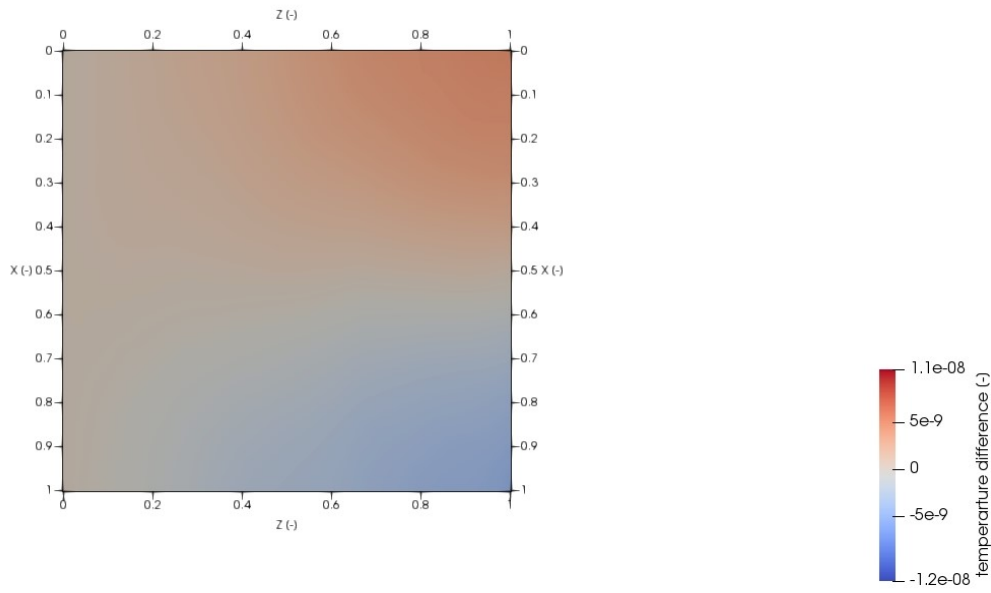


Figure 34: Slice normal to the y-axis on the homogeneous steady Fourier Simulation

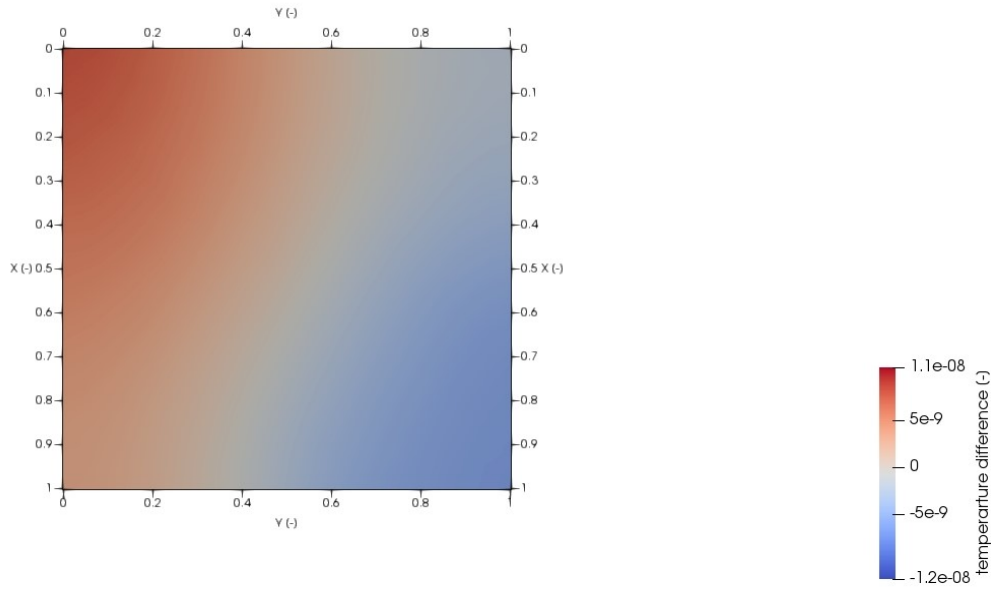


Figure 35: Slice normal to the z-axis on the homogeneous steady Fourier Simulation

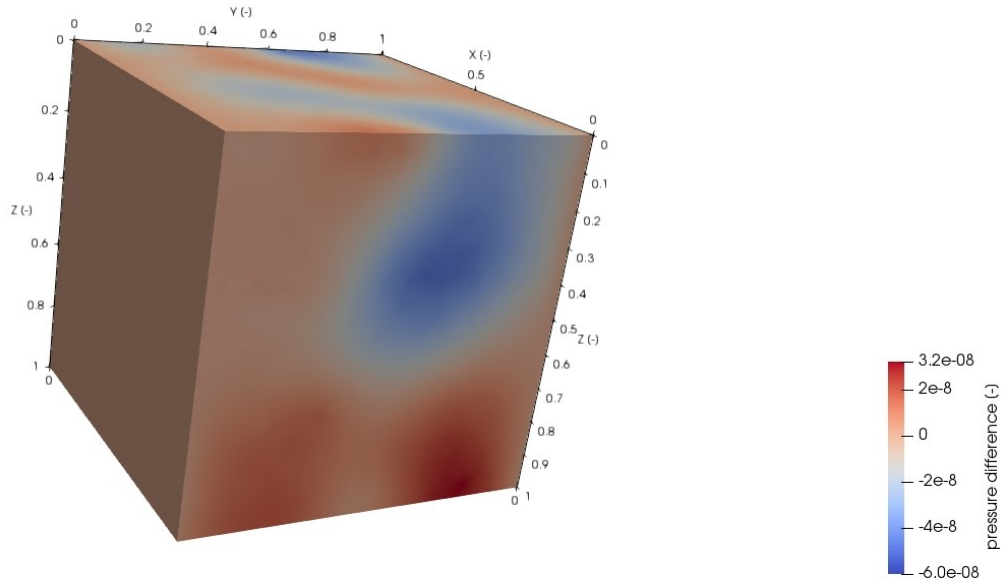


Figure 36: Steady State Darcy Difference Plot for the homogeneous Simulation

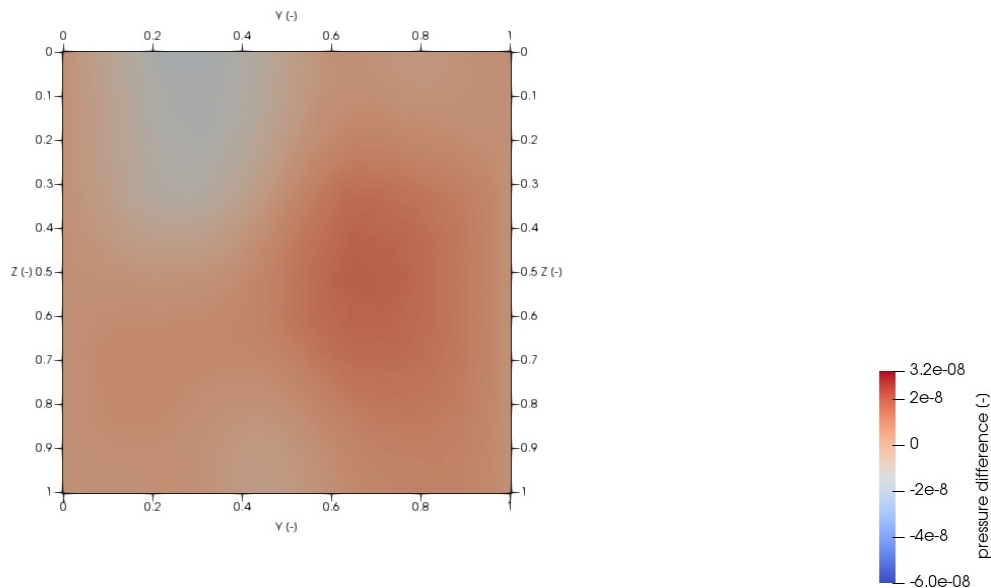


Figure 37: Slice normal to the x-axis on the homogeneous steady Darcy Simulation

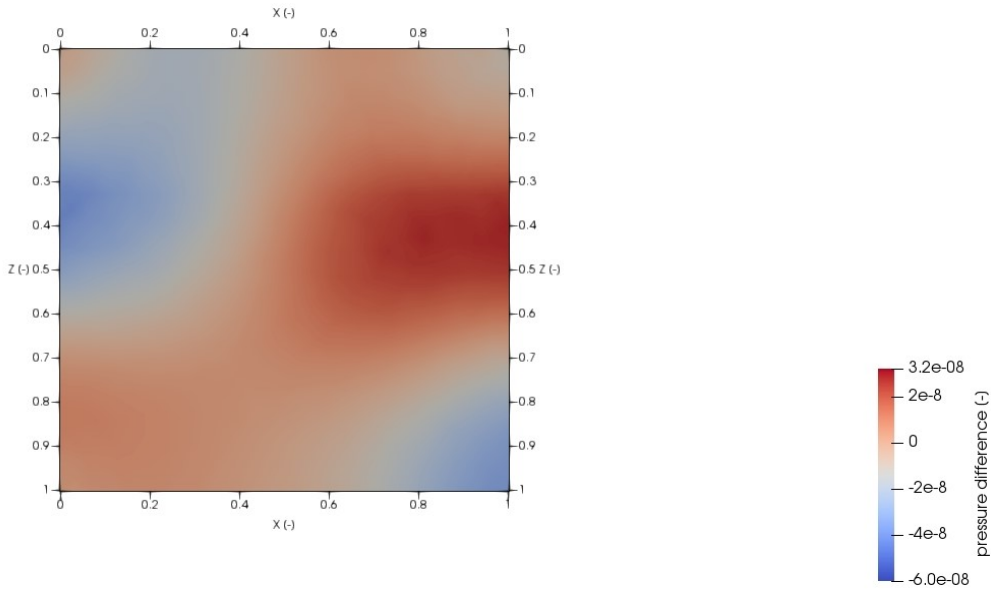


Figure 38: Slice normal to the y-axis on the homogeneous steady Darcy Simulation

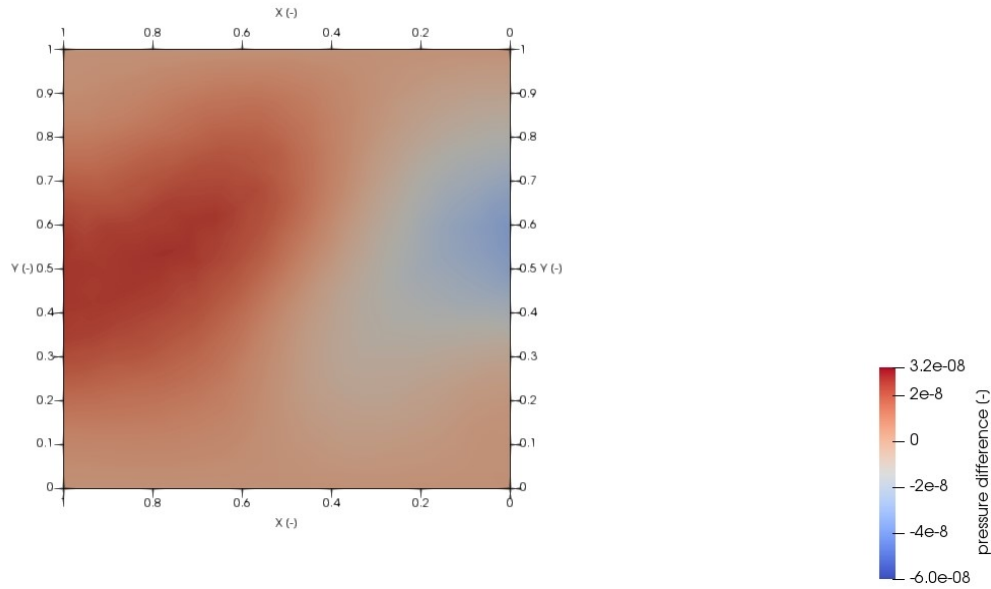


Figure 39: Slice normal to the z-axis on the homogeneous steady Darcy Simulation

A.3 Python Code for Theis Solution

```

# Python Code for Theis Solution Nickname: 'Penguin'

# import modules

import numpy as np
import matplotlib.cm as cm
import math
import matplotlib.pyplot as plt
import matplotlib

# Define Constant Values

Q = 0.002 #production rate [m^3/s]
S = 0.005 # storativity [-]
K = 6*10**(-4) # hydraulic conductivity [m/s]
hm = 25 # groundwater filled aquifer thickness [m]
T = K*hm #transmissivity in [m^2/s]

#Timesteps

#timesteps = np.logspace(5,12,10) #t_start , t_end , n curves , logarythmic
timesteps =np.linspace(100000,400000,4) #t_start , t_end , n curves , linear

#Radius

r = np.arange(1,1001, 1) #[m]

#Well Function

def Wu(u,n):
    a = (-0.5772) - np.log(u)
    for i in range(1,n+1):
        a -= (-1)**i * u**i / (i*math.factorial(i))
    return a

#Full Equation

def gen(t,r):
    u = ((r**2)*S) / (4*T*t)
    W = Wu(u,6)
    hrt = (Q*W / (4* math.pi * T))
    return hrt

#Data Plotting

plt.figure(figsize=(10, 10))

```

```

#Colors for the Curves

color=iter(cm.rainbow(np.linspace(0,1,len(timesteps)))))

#Data Plotting Drawdown

for timestep in timesteps:
    plt.plot(np.true_divide(r, hm),np.true_divide(gen(timestep,r),
        hm),c=next(color), ls='--', label='t={}'.format(timestep))

#Basic Graph Traits

plt.ylim(0,None)
plt.xlim(0,None)
plt.legend(loc=2)
plt.xlabel("Distance[-]")
plt.ylabel("Drawdown[-]")
plt.gca().invert_yaxis()

# Grid Plotting

plt.grid()
plt.grid(b=True, which='major', color='k', linestyle='-')
plt.grid(b=True, which='minor', color='k', linestyle='--', alpha=0.2)
plt.minorticks_on()

# Plot Axis Position

ax = plt.gca()
ax.xaxis.set_ticks_position('top')
ax.xaxis.set_label_coords(0.5, 1.075)

plt.plot()

```